Earth's Future

RESEARCH ARTICLE
10.1029/2022EF003118

Special Section:
CMIP6: Trends, Interactions, Evaluation, and Impacts

Future Changes in Tropical Cyclone Exposure and Impacts in Southeast Asia From CMIP6 Pseudo-Global Warming Simulations

Thao Linh Tran[1,2], Elizabeth A. Ritchie[3], Sarah E. Perkins-Kirkpatrick[1], Hai Bui[4], and Thang M. Luong[5]

[1]School of Science, and ARC Centre of Excellence for Climate Extremes, University of New South Wales, Canberra, ACT, Australia, [2]Institute for Climate, Energy & Disaster Solutions, and Research School of Earth Sciences, and ARC Centre of Excellence for Climate Extremes, Australian National University, Canberra, ACT, Australia, [3]School of Earth, Atmosphere and Environment, and Department of Civil Engineering, Monash University, Clayton, VIC, Australia, [4]Geophysical Institute, University of Bergen, Bergen, Norway, [5]Climate Change Center, King Abdullah University of Science and Technology, Thuwal, Saudi Arabia

Abstract In this Pseudo-global Warming study, potential future changes in the Southeast Asia tropical cyclone (TC) exposure climatology are quantified. One hundred and seventeen landfalling TCs in the last 20 years are simulated with their current climate conditions and also with the Coupled Model Intercomparison Project Phase 6 (CMIP6) ensemble perturbed conditions under the SSP2-4.5 and SSP3-7.0 climate change scenarios. Our simulations suggest that landfalling TCs are projected to be 8% more intense at landfall, 2.8% faster and have smaller sizes by the end of the 21st century under the SSP3-7.0 scenario. In addition, TC landfall locations shift northward with tracks extending further inland toward Laos and Thailand. In particular, TC exposures, wind and rainfall impacts significantly increase in the northern Philippines, Taiwan, southwestern coast of China, and northern Vietnam; and significantly decrease in the southern areas of Southeast Asia and the southeastern coast of China.

Key Points:

- Tropical cyclones are projected to be more intense, smaller in size, and to move faster
- Landfalling locations shift poleward and further west by the end of the 21st century
- Wind and rain impacts increase in the northern Southeast Asia, extend further inland

Supporting Information:

Supporting Information may be found in the online version of this article.

Correspondence to:

T. L. Tran,
thaolinh.tran@anu.edu.au

Citation:

Tran, T. L., Ritchie, E. A., Perkins-Kirkpatrick, S. E., Bui, H., & Luong, T. M. (2022). Future changes in tropical cyclone exposure and impacts in Southeast Asia from CMIP6 pseudo-global warming simulations. *Earth's Future*, *10*, e2022EF003118. https://doi.org/10.1029/2022EF003118

Received 17 AUG 2022
Accepted 15 NOV 2022

1. Introduction

Situated on the western edge of the western North Pacific (WNP), Southeast Asia is characterized as among the highest tropical cyclone (TC)-prone areas with approximately 42 million people exposed to TC hazards (United Nations, 2021). According to the United Nations (2021), the vast majority of TC-induced mortalities in Asia and the Pacific in the 2000s and 2010s were from this region. TC risks are of concern in Southeast Asia because of changes in TC exposure over the last 50 years. Tran et al. (2022) observed an increasing landfalling TCs tendency in this region during 1970–2019 using the Joint Typhoon Warning Center (JTWC) data set and a northward shift in landfalling TC locations between the first and last 25 years in four agency best track records. Quantifying potential trends in the physical properties of Southeast Asia landfalling TCs (SEAL-TCs) under reasonable climate change scenarios is, therefore, an imperative need for TC risk management and adaptation for the region.

In recent decades, substantial efforts have been made to improve confidence in projections of TC characteristics in the WNP. Most projections consistently suggested that WNP TCs will increase in intensity with a median change of +5% under a 2°C global warming scenario by the end of the 21st century (Cha et al., 2020). Tsuboki et al. (2015) suggested that Japan might be affected by more extremely intense supertyphoons (STYs) with an increase of 19% in the maximum wind speed and a decrease of 2.3% in minimum central pressure as sea surface temperature (SST) increases under the A1B scenario used in Coupled Model Intercomparison Project Phase (CMIP) 3. Lok and Chan (2018) projected that fewer but stronger TCs would make landfall in South China by the end of the 21st century under the Representative Concentration Pathway 8.5 (RCP8.5) scenario used in CMIP5. Chen et al. (2020) found shorter return periods of TC extreme winds in the Mekong river basin by 2081–2100 under the RCP8.5 scenario, with higher risks concentrated in coastal areas. While many studies examined the response of TC intensity to global warming on the basin (e.g., Knutson et al., 2015), sub-regional (e.g., Chen et al., 2020) or country (e.g., Lok & Chan, 2018) scales, an investigation on future changes in inland wind impacts caused by SEAL-TCs that is critical to effective preventative and mitigating controls in the region has not been conducted.

The most popular agreement among current studies (e.g., Kanada et al., 2013; Knutson et al., 2015; Tu et al., 2021; Villarini et al., 2014; Yamada et al., 2017) is a projected increase in the rainfall associated with WNP TCs. A median rainfall increase of 17% for projections after being rescaled to a 2°C global warming scenario is suggested (Cha et al., 2020). In an extreme case, Tsou et al. (2016) found that the rain rate within 200 km of the TC center near Taiwan and the East China Coast increased by 54%, which is almost 2.5 times more than for the whole WNP basin (+22%) in the late 21st century under the RCP8.5 scenario. This increasing TC rain rate along with sea level rises will likely exacerbate the combined storm fresh- and salt-water inundation in the WNP region (Cha et al., 2020). Apart from reasonable estimates for increasing TC rain rate, it is also important to examine the geographical distribution of TC accumulated rainfall, which is determined by the spatial TC rain extent and duration for realistically assessment of future TC rain impacts. This implies that TC rain projections need to be more thoroughly investigated in association with changes in TC size, track, and landfall patterns, as well as translation speed.

Current projections for TC size varies considerably in available projections. In response to ocean warming, the spatial extent of WNP TCs is projected to increase in Sun et al. (2017), Yamada et al. (2017), while a decrease by 8% is shown in the study of Knutson et al. (2015). Within the TC inner-core, Kanada et al. (2013) found a reduction in the radius of maximum wind speed under the warming SST conditions forced by the A1B scenario. The impacts of climate change on TC translation speed, which will affect the duration of TC rain and winds over an area, are also not well elucidated in the literature. Emanuel (2021) projected a significant slowdown in TC translation speed in the subtropics with a hybrid statistical downscaling framework applied to CMIP6 models, but no significant change in the tropics. There is no clear signal for a change in TC motion globally (Kim et al., 2014), in the North Atlantic (Knutson et al., 2013) or the WNP (Wu et al., 2014).

Among available projected changes in TC tracks, a few similar attributes can be pointed out for the WNP including an eastward shift in tracks to the central Pacific (Cha et al., 2020; Knutson et al., 2020), and a northward shift in tracks, which may produce changes in TC exposure regions in the basin (Korty et al., 2017; Kossin et al., 2016; Lok & Chan, 2018; Nakamura et al., 2017; Wu et al., 2014). However, there is low confidence in TC track projections because of: (a) the absence of a detectable human-induced TC track trend in the past; (b) the inherent bias in regional SST projections, which affect the future climate projections; and (c) a weak consensus among projections (Knutson et al., 2020). It is particularly important to be able to produce TC tracks with sufficient confidence using climate projections since TC impact quantification is greatly influenced by their tracks.

Most of the available TC projections in the WNP basin investigate how TC physical characteristics respond to changes in individual climate parameters such as SST or environment warming in isolation (e.g., Nakamura et al., 2017; Sun et al., 2017; Yamada et al., 2017). While one can argue that the thermodynamic conditions dictate the response of the momentum fields in the long term, this assumption may not be correct for the studies using short-term simulations. In fact, a variety of oceanic and atmospheric parameters were demonstrated to be critical to TC development and intensification including SST (e.g., Emanuel, 1999; Holland, 1997), fluxes and wind speeds at the surface (Emanuel & Sobel, 2013), or unstable environment conditions and weak wind shear (Trenberth et al., 2018).

In summary, there is a lack of studies on how landfalling TCs and their associated impacts in Southeast Asia will potentially change in the future. In this study, we propose to fill in the gap by employing the pseudo-global warming (PGW) framework to examine changes in the characteristics of the present-day landfalling TCs in the warming climate. The PGW framework is chosen to avoid issues with directly downscaling from the typically poor TC signals from global climate models (GCMs) (e.g., Camargo, 2013). Very importantly, for the first time, concurrent impacts of future changes under climate change scenarios used in CMIP6 with a comprehensive set of the most important oceanic and atmospheric parameters for TC activity (i.e., SST, atmosphere temperature (Ta), relative humidity (RH), winds) are taken into consideration.

To construct the landfalling TC climatology in different climate states, a sufficiently large TC sample is required for a meaningful analysis. In this study, 117 TCs from 1999 to 2018 across varieties of intensities and sizes representing the climatology of the SEAL-TCs were simulated in the present climate plus six other climate states from three future periods (i.e., the 2030s, 2050s, and 2090s) under two climate forcing scenarios (i.e., a medium SSP2-4.5 and an aggressive SSP3-7.0). This resulted in 819 high-resolution simulations in total produced using the Weather Research and Forecasting (WRF) model driven by the CMIP6 ensemble average perturbed conditions. These simulations present an unprecedented database of TC-related climate forcing simulations to investigate the

impacts of climate change on SEAL-TCs. Investigation of the variations among simulated climate states offers insight into the range of possible changes both for TC attributes and related wind and rainfall impacts in Southeast Asia by the end of the 21st century.

Following is the structure of the paper. In Section 2, details of CMIP6 and validation data, the PGW technique, experiment design, and analysis methods are presented. Simulation results of TC characteristics, rainfall, and wind impacts among climate states are discussed in Section 3. Section 4 provides a summary, discussions, and conclusions.

2. Data, Methodology and Experimental Design

2.1. Data

In this study, the NCEP Final Operational Model Global Tropospheric Analyses (FNL) data set at 1° × 1° horizontal resolution (available at https://rda.ucar.edu/datasets/ds083.2/#description) was used as the input data to simulate SEAL-TCs in the current climate conditions (control run simulations—hereafter CTR). Data from the JTWC best track archive provided in IBTrACS version 4.0 (Knapp et al., 2018) including TC position, maximum wind, minimum pressure, the critical wind radii of 34-, 50-, 64-kt winds (hereafter, *R*34, *R*50, *R*64) are used to evaluate the CTR simulated TC tracks, intensities, and size. The Tropical Rain Measurement Mission (TRMM) 3B42 v7 data set gridded with a spatial resolution of 0.25° (covering 50°S–50°N), and 3 hourly temporal intervals (Greenbelt, 2011) are used to assess the simulated TC-rain impacts.

Future climate change signals are derived from the CMIP6 models under two contemporary scenarios including SSP2-4.5 and SSP3-7.0 (Meinshausen et al., 2020). While SSP2-4.5 contains the same magnitude of an increased radiative forcing at 2100 of 4.5 W m^{-2} as RCP4.5, SSP3-7.0 with a radiative forcing of 7.0 W m^{-2} is new compared with RCPs used in CMIP5. These medium (SSP2-4.5) and aggressive (SSP3-7.0) scenarios, in turn, project a mean global warming of 3.0 and 4.1°C, respectively by the end of the 21st century (O'Neill et al., 2016). These scenarios are being used in this study due to a more realistic range of future forcing pathways compared to the "business as usual" scenario (SSP5-8.5) (Hausfather & Peters, 2020). The scenarios are based on not only assumptions about socioeconomic, technical developments, and environmental conditions, but also consider global commitments on carbon emission reduction from the Paris Agreement. Three future periods are selected for analysis including the near-future (2030s), mid-future (2050s), and far-future (2090s) represented by the average of 2025–2034, 2045–2054, and 2085–2094 periods, respectively. The current climate (2010s) is represented by the average of the 2005–2014 period. Twenty-eight CMIP6 models which have available data for the two selected scenarios in the chosen periods at the time of data collection are chosen (Table S1 in Supporting Information S1).

2.2. Pseudo-Global Warming Technique

The PGW framework was first proposed by Schär et al. (1996), then widely applied in TC studies investigating changes in the behavior of present-day TCs in future climate change conditions (e.g., Gutmann et al., 2018; Hill & Lackmann, 2011; Lackmann, 2015; Lynn et al., 2009; Mittal et al., 2019; Nakamura et al., 2016; Parker et al., 2018; Reddy et al., 2021). In this method, the present large-scale environment that contains TCs is perturbed by climate change signals from GCMs, and then used as initial and boundary conditions for a high-resolution regional climate model to simulate future TC attributes (e.g., Parker et al., 2018). In this study, the present conditions are obtained from the FNL data set, and climate change signals (hereafter, climate deltas) are derived from 28 CMIP6 models (Table S1 in Supporting Information S1).

To calculate the climate deltas, "climate means" of a given period (i.e., 2010s, 2030s, 2050s, 2090s) and climate change scenario (i.e., SSP2-4.5, SSP3-7.0) are first calculated for five variables including SST, Ta, RH, zonal and meridional wind speed (U, V) (e.g., Figure S1 in Supporting Information S1), which are important to TC thermodynamic processes and movement (Gutmann et al., 2018). The use of the means of a sufficient number of CMIP6 models is to minimize possible biases and/or large internal variations from each individual model (e.g., Rasmussen et al., 2011; Redmond et al., 2014) (e.g., Figures S2a–S2d in Supporting Information S1). Those "climate means" are then used to define climate deltas by applying

$$\Delta\overline{\phi}_P = \overline{\phi}_P - \overline{\phi}_{2010s}, \quad (1)$$

Table 1
Experimental Design

Experiment	Period	Scenarios	$\overline{\Delta SST}$	$\overline{\Delta RH}$	$\overline{\Delta T_a}$
CTR	1999–2018	–	–	–	–
med2030s	2025–2034	SSP2-4.5	+0.35	+0.09	+0.97
med2050s	2045–2054	SSP2-4.5	+0.72	+0.10	+1.95
med2090s	2085–2094	SSP2-4.5	+1.29	+0.27	+3.21
high2030s	2025–2034	SSP3-7.0	+0.39	+0.12	+0.99
high2050s	2045–2054	SSP3-7.0	+0.86	+0.24	+2.17
high2090s	2085–2094	SSP3-7.0	+2.01	+0.56	+4.90

Note. The averaged climate delta is taken over the Southeast Asia D01 domain for SST, RH at 500 hPa, and Ta at 300 hPa.

where P is a 10-year period in the future, and $\overline{\phi}_P$ is the monthly average over the period P. The magnitudes of changes in SST, RH, Ta for the future periods and scenarios from present climate conditions are shown in Table 1 and an example for SSP3-7.0 is in Figure S1 in Supporting Information S1.

Next, the perturbed data ϕ_P used as the input for the WRF model are defined by adding the resultant three-dimensional climate deltas to the corresponding variables from the FNL data set using

$$\phi_P = \phi_{FNL} + \Delta\overline{\phi}_P \quad (2)$$

Note that as the oceanic and atmospheric grids of the chosen CMIP6 models are at different resolutions (Table S1 in Supporting Information S1), data were all interpolated to the same 1° grid resolution of the FNL reanalysis before the climate means and climate deltas were calculated.

2.3. WRF Model and Simulation Design

2.3.1. WRF Model

We used the Advanced Research version of the WRF model (WRF-ARW), version 4.1.3 (Skamarock et al., 2019), for the simulations. To realistically simulate TC physical structure, a model horizontal resolution of 4 km or higher is recommended (Gentry & Lackmann, 2010). Instead of a uniformly high-resolution domain, which has high computing costs, the WRF-ARW vortex-following nested grids were implemented in this study as a strategic cost-effective alternative. The grid system was set up to include a large coarse static grid (D01) covering the whole Southeast Asia region (85.3°E–144.7°E, 6.7°S–40.3°N), and two small finer vortex-following nested grids (D02 and D03). Their dimensions are 6,282 × 5,382, 1,440 × 1,440, and 282 × 282 (east-west × north-south) km^2 with spatial resolutions of 18, 6, and 2 km, respectively. The model uses 43 vertical levels with its top pressure set at 50 hPa.

Figure 1 demonstrates the grid system by showing a snapshot of 700 hPa geopotential height for STY Haiyan at 06 UTC, 9 November 2013. The innermost 2-km grid (D03) covers the inner core region of the cyclone and resolves the detailed eyewall convective structure. The intermediate 6-km grid (D02) captures the cyclone's circulation and the outermost grid (D01) provides the large-scale environmental conditions downscaling from the perturbed FNL forcing data. We used two-way interactions between grids so that the coarser grid receives information from better-resolved processes in the finer grid. The center of D03 is initially located at the TC center from the JTWC data set and the nested grid boundaries are set to be at least 450 km from the mother grid boundaries. This setting not only enables the nested grids to flexibly follow the cyclone during the integration despite variations in the TC motion, but also ensures that the cyclone circulation and its inner-core remain located in the middle of the higher resolution D02, and D03 domains, respectively.

For the physics and dynamic options, we set up a sensitivity experiment with different physical parameterization schemes for a typical strong landfalling TC in the region named Wutip (2013) to determine an appropriate model configuration in simulating the TC track and intensity (result not shown). The resulting configuration for all domains in this study includes the Morrison 2-moment microphysics scheme (Morrison et al., 2009), the UW planetary boundary layer scheme (Bretherton & Park, 2009), the Kain-Fritsch cumulus parameterization scheme (Kain, 2004), the Rapid Radiative Transfer Model longwave radiation scheme (Mlawer et al., 1997), and the Dudhia shortwave radiation scheme (Dudhia, 1989). The cumulus scheme is turned off for the finest domain (D03) so that convection is only modeled using the explicit deep convection calculation scheme on D03.

Incorporating the climate deltas into the initial conditions of a model may cause dynamical imbalances that affect the simulation results (Parker et al., 2018). We alleviate this issue by applying the WRF digital filter initialization (DFI) procedure (Lynch & Huang, 1992) to the initial conditions with an adiabatic backward and adiabatic forward integration (Peckham et al., 2015). We tested the efficiency of the DFI settings for six historical TCs with variate intensities using the DFI durations of 1 or 2 hr. The initial conditions for TCs were best represented in the 2-hr DFI simulations with the most symmetric TC structure and strongest precipitation intensity (e.g., Figure S3 in Supporting Information S1). DFI procedures improve the track forecasting for both setups (Figure S4 in

10.1029/2022EF003118

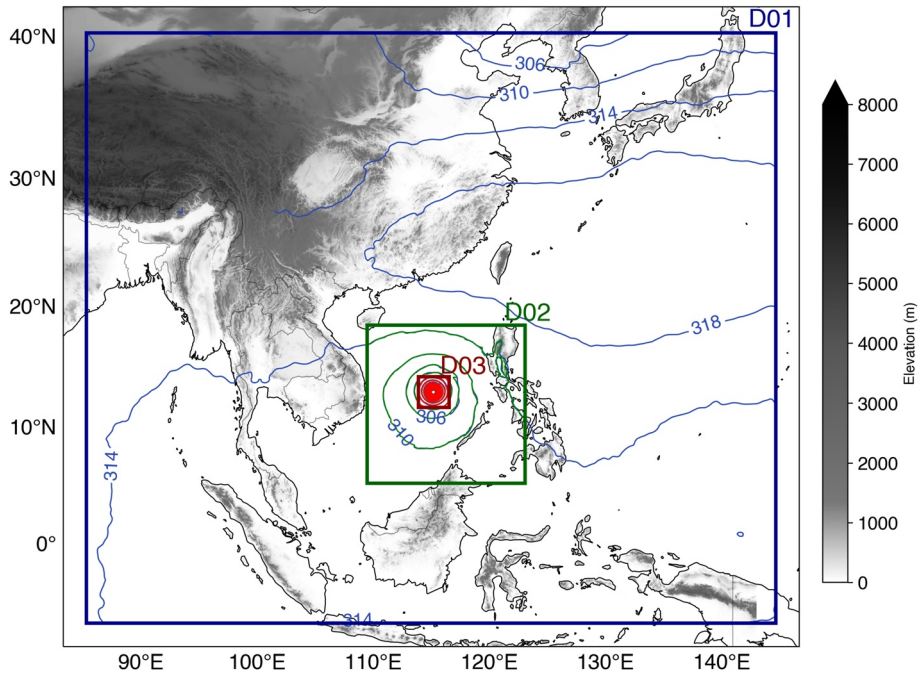

Figure 1. A snapshot of 700 hPa geopotential height at 06 UTC 9 November 2013 for the case of supertyphoons Haiyan (2013) with the three Weather Research and Forecasting domains. The blue, green and red contours represent data from the coarsest (D01—18 km), intermediate (D02—6 km) and finest (D03—2 km) grids, respectively. The background topography are obtained from the ETOPO1 1 arc-minute global relief model (NOAA, 2009).

Supporting Information S1). We ultimately opted for the 2-hr DFI for the final WRF configuration. In addition, spectral nudging (e.g., Feser & Storch, 2008; Omrani et al., 2012; Storch et al., 2000) is also implemented to preserve the variability of the large-scale circulation, such as ridges and troughs, from the driving global model (e.g., Castro et al., 2012) by nudging features with wavelengths of approximately 2100 km and greater in the coarsest domain (D01).

2.3.2. Simulation Design

We first simulated all 307 SEAL-TCs between 1999 and 2018 using current atmospheric conditions directly from the FNL reanalysis data (CTR). In most cases, we initialized the simulation after the TC genesis to avoid stochastic variations that complicate the comparisons among different climates (e.g., Done et al., 2014; Gutmann et al., 2018). There were exceptions to this such as some TCs that formed close to land, which required early simulations to capture early overland impacts. Finally, the termination time for every simulation was set 48 hr after the final recorded time in the JTWC best track to capture: (a) continuing impacts after the system was no longer intense enough to be tracked by JTWC; and (b) any future climate effect that might extend the life of the TCs.

Because of the coarse resolution of the FNL, some TCs are not well resolved in the initial conditions and cannot develop properly without using a TC initialization technique. These TCs were not being selected resulting in a set of 170 TCs at this filtering step. This set is then used in future PGW simulations (Table 1). Additional quality control checks were conducted to keep only the TCs whose tracks were reasonably simulated in all six future states. In particular, any case in which the WRF nests failed to properly track the simulated TC were excluded. As a result, a final control simulation set of 117 TCs including a wide range of intensities from weak tropical depressions to intense STYs is used in final analyses (Table S2 in Supporting Information S1). The final data set, therefore, contains a total of 819 simulations (117 TC events × [1 control + 6 perturbed experiments]), which were used to examine changes in the Southeast Asia TC landfall and impact climatology.

2.4. Post Simulation TC Tracking

The default vortex-following tracker in WRF was initially used to track TCs in the model outputs. However, when the cyclone moved over complex topography and weakened, the automated WRF sometimes switched to follow a stronger low-pressure system that might also co-exist within the model domain and provided false tracking information. Several existing trackers (e.g., Au-Yeung & Chan, 2012; Heming, 2017; Reddy et al., 2021; Takahashi & Yasunari, 2008) were also tested, but none of them consistently tracked all TCs from the 819 simulations. Thus, we developed a new objective center-finding algorithm to realistically track the simulated TCs.

The first step of this new tracking procedure is to merge the model output from all three grids into the D01 domain by replacing the values on the outer grids with those of the finer grids where they are available. Next, the 700-hPa geopotential height field is smoothed using a convolution filter (Astropy Collaboration et al., 2018) to eliminate small perturbations, especially over complex topography, while retaining the TC circulation. A first-guess TC center is then being located at the grid point with minimum 700-hPa smoothed geopotential height within a search radius of 330 km from the TC center at the previous time step. Once the first-guess TC center is determined, it must satisfy the following criteria: (a) the mean sea-level pressure is less than 1,000 hPa; (b) a closed isohypse of 700-hPa geopotential height exists, which means there are at least eight points on a radius ranging from 200 to 300 km around the minimum point with geopotential height values of at least 20 dm larger than that of the TC center. This is an adjustment of the isobar check used at the UK Met Office (Heming, 2017); and (c) the maximum relative vorticity at 700 hPa within the search radius from the first guess point exceeds 30×10^{-4} s^{-1}. If all the criteria are satisfied, the TC center is found and the next time step will be proceeded, otherwise, the tracking process is terminated.

The above thresholds were determined to enable the tracker to detect and track the TC remnant low as long as it still resembles a cyclone. However, in a few cases of un-named TCs, the TC becomes too weak for even these criteria to automatically track. In those specific situations, we relaxed the mean sea-level pressure and relative vorticity criteria to 1,004 hPa and 15×10^{-4} s^{-1}, respectively, to capture the weak TC remnants to assess the possible rain impacts.

2.5. Analysis Technique and Significant Tests

A variety of TC characteristics were calculated based on the TC trajectory and its wind distribution including the translation speed, spatial track density, TC inner-core size, and the whole circulation size. Translation speeds are computed by dividing the distance between each two consecutive TC center points along the track by the 3-hr interval time. The values of all time intervals are averaged for the final translation speed of the TC. The track density (D) is calculated for all the grid points (with a grid size of 0.5°) by adding an impact factor for every TCs record. The impact factor is a function of the distance from the grid point to the TC center (r). In the most simple case proposed by Hart and Evans (2001), this impact factor is equal to 1 within the impact radius R_i, which is 300 km, and zero outside.

$$f(r) = \begin{cases} 1, & \text{if} \quad r \le R_i \\ 0, & \text{if} \quad r > R_i \end{cases} \tag{3}$$

A more realistic approach is to define the impact factor as 1 at the TC center, then gradually reduces to 0 at the impact radius (Leary & Ritchie, 2009). In the current study, the impact factor function is defined as follows:

$$f(r) = 1 - \frac{r}{R_i}, \tag{4}$$

where the impact radius $R_i = 300$ km.

Changes in TC structure in the future climate scenarios are assessed using the radii of 25-kt (hereafter, Rt_{25}) and maximum (hereafter, $Rt_{\max}$) tangential winds at the lowest model level (i.e., approximately 25 m above the ground level on average), representing the outer (e.g., Kim et al., 2014) and inner-core sizes (e.g., Kilroy et al., 2016), respectively. The use of tangential winds is to reduce influences from environmental flow following Kim et al. (2014).

For each critical wind speed of 34, 50, and 64 kts, we define the wind impact distribution as the frequency of the 10-m wind exceeding the corresponding critical value. This method can be applied to the WRF gridded wind data output in which only grid points with wind speeds larger than given thresholds are included in the calculation. Hereafter, we denote these as the realistic calculations of wind impact with WI_{34}, WI_{50}, and WI_{64}. Meanwhile, for the best track data, the only information available are the corresponding critical wind radii R_{34}, R_{50}, and R_{64}. Thus, wind impacts are calculated using Equation 3, where the impact radius R_i are replaced by the critical wind radii R_{34}, R_{50}, and R_{64}. We denote these as simplified calculations with WI_{34s}, WI_{50s}, and WI_{64s}. For the model validation purpose, we also applied the simplified calculation of wind impacts to the WRF simulations, where the critical wind radii in the model are computed from the 10-m wind speed.

To assess changes in the extreme intensities, the lower and upper ranges are defined by the rule of 1.5× inter-quantile range. Given inter-quartile range and quartile in turn denoted by IQR and Q, extreme $V_{\max}$, V_{lf} are derived from $75thQ + 1.5 \times IQR$, and extreme Pc are derived from $25thQ - 1.5 \times IQR$. Variations in the TC overall wind energy and TC landfalling activity are evaluated via the accumulated cyclone energy (ACE) (Waple et al., 2002), and the annual power dissipation index (APDI) (Liu & Chan, 2017), which were calculated as:

$$ACE = \frac{\sum_{i=1}^{n} V_{max6}^2}{10^4}, \tag{5}$$

$$APDI = \sum_{i=1}^{n} V_{lf}^3 \tag{6}$$

where V_{max6} is the maximum wind speed during each 6-hr interval, V_{lf} is the intensity at landfall, and n is the number of values. Here, following Tran et al. (2022), a TC landfall is counted whenever the TC center crosses the Southeast Asia coastline (defined by the Natural Earth coastline data set at a scale of 1:50 million) from sea to land. Note that all landfalls by a TC and all TCs were included in the calculation of Equation 6.

Further investigation on the TC destructive potential was conducted via computing Integrated Kinetic Energy (IKE) (Powell & Reinhold, 2007) which considers the entirety of a TC's surface wind field following Kreussler et al. (2021):

$$IKE = \int_v \frac{\rho U^2}{2} dV = \frac{1}{2} kgm^{-2} \times \int_A U^2 \, dA \tag{7}$$

where the air density is uniformly equal 1 kg m^{-3}, and U is 10-m wind speed exceeding 25 kts at grid points within 1,000 km of the TC center. The 25-kt threshold was chosen to include weak TCs in the IKE assessment. IKE was computed at landfall moments, then accumulated throughout all simulated TCs.

In this research, TC-related rain impacts are defined as precipitation falling overland within a radius of 500 km of the TC center accumulated over the lifetime of each TC and throughout all TCs simulated. Although the spatial extent of TC rain varies among TCs and is associated strongly with the TC intensity (e.g., Jiang et al., 2008; Niu et al., 2022; Touma et al., 2019), the radius of 500 km is widely used in previous literature examining TC rain (e.g., Englehart & Douglas, 2001; Khouakhi et al., 2017; Prat & Nelson, 2013; Ritchie et al., 2011; Wood & Ritchie, 2013) as this generally captures rainfall associated with the eyewall, inner and outer core rainbands of TCs (e.g., Dare et al., 2012; Rodgers et al., 2001).

The two-sample Kolmogorov-Smirnov test (KS-test 2) (Massey, 1951) is applied to reject the null hypothesis that the values of TC intensity, radii, and translation speed between current and future climate simulations, are from the same cumulative distribution. In addition, the Permutation test (Phipson & Smyth, 2010), which does not require any assumption about the underlying distribution shape for data, is utilized to statistically test the significant changes in the mean value of key TC metrics. The significance of changes in TC physical impacts in the future is tested using the Wilcoxon signed-rank and rank-sum tests (Wilcoxon, 1992). In particular, the Wilcoxon signed-rank test, which assumes two dependent samples, was used to test the significance of the difference in the medians of the impact factor of the current and each future climate state simulation. The sample sizes are large enough to be considered as matched samples. Meanwhile, the Wilcoxon rank-sum test, which tests independent samples, was applied to wind and rain impacts whose sample sizes are much smaller. The Wilcoxon signed-rank test tends to provide more significance than the Wilcoxon rank-sum test.

10.1029/2022EF003118

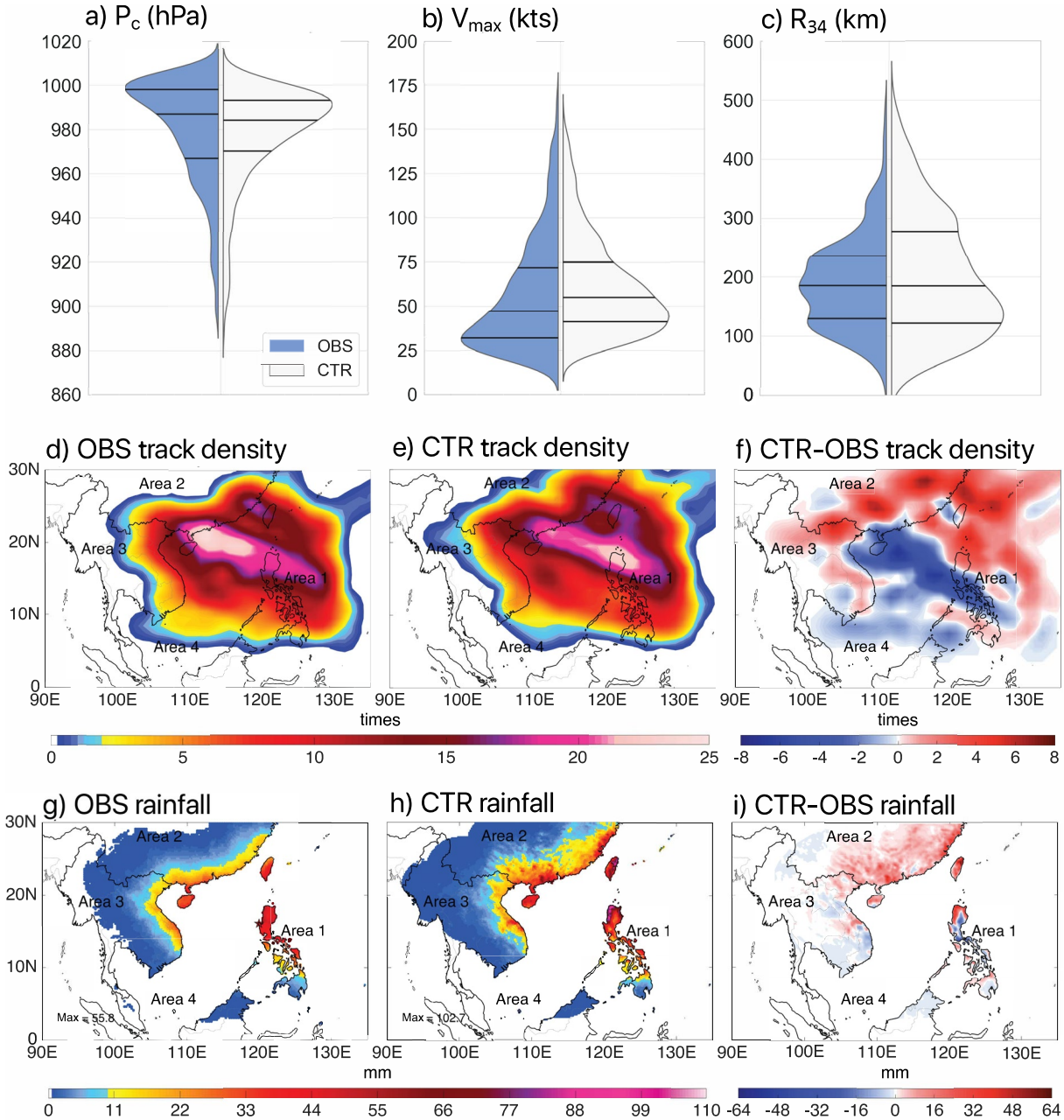

Figure 2. Comparisons between the observed (OBS) and Weather Research and Forecasting simulated (CTR) tropical cyclone (TC) metrics includes: the violin plots for OBS and CTR of (a) central pressure (Pc), (b) maximum wind (V_{max}), and (c) size (R_{34}); Track density for (d) OBS, (e) CTR and (f) the difference CTR–OBS; Normalized accumulated rainfall for (g) OBS, (h) CTR, and (i) CTR–OBS difference. In (a–c), the lower, middle, and upper black solid lines in each violin indicate the 25th, 50th and 75th percentiles, respectively. In (g–i), the rainfall in each grid point is normalized by the total number of landfalling TCs during the period.

3. Results

3.1. Model Validation

A good performance in reproducing TC activity at the present climate of the modeling system implies a higher confidence for future projections (Seneviratne et al., 2021). The distributions of SEAL-TCs intensity between the IBTrACS (OBS) and WRF simulations (CTR) are compared in Figures 2a and 2b. The distributions of central pressure (Pc) and maximum wind between the CTR and OBS suggest reasonable agreement. Generally, slightly lower minimum pressures and higher maximum winds indicating higher intensities were produced by the WRF model compared to observations (Figures 2a and 2b). Despite simulating a smaller value for the lowest central

pressure (Figure 2a), WRF did not capture the most extreme wind speed values around 170–175 kts observed in IBTrACS (Figure 2b). The 2-km resolution of these WRF simulations might be not fine enough to simulate the highest wind speeds. Previous studies (e.g., Davis et al., 2008; Lind et al., 2016) demonstrated that regional climate models typically cannot resolve the most extreme motions even with horizontal resolutions of 1–2 km.

Figures 2d–2f shows the distributions of the track density for OBS and CTR and their difference from 1999 to 2018. To some extent, WRF reasonably simulates the spatial extent of track density of the SEAL-TCs, notably the prevailing northwest-southeast belt from the Philippine East Sea to the southern China coast. High TC impact near Taiwan and the center of Vietnam are also captured, although anomalies over the southern China coast (northern Philippines) are underestimated (overestimated). Compared to the best track, there is higher TC exposure further inland in southern China, along Vietnam, and in Myanmar. This behavior can be explained by the design of the new automatic tracker to also capture remnant TC low tracks, which are not normally recorded in the IBTrACS.

In terms of TC rainfall, the spatial distribution of TC rain simulated by WRF is generally similar to the TRMM observations with the highest accumulated rainfall in the Philippines and Taiwan, less intense rain along the Southeast Asian coast, and considerable decreases over areas more than 200 km from the coast (Figures 2g–2i). However, the peak simulated values in eastern Taiwan and northern Philippines are nearly double that observed, and much higher rain amounts are also found in the Southeast Asian mainland along China and Vietnam reaching further inland in the WRF simulation. Extreme rainfall is typically underestimated by TRMM due to its coarse (0.25°) resolution (e.g., Chang et al., 2013). Thus, it is reasonable to expect higher rainfall amounts from the 18 km spacing static grid of WRF. Moreover, since the 2-way nesting option is turned on in the WRF simulations, thermodynamical feedback from the 6-km and 2-km nests probably also contribute to the larger rainfall amount in the outermost WRF domain to some extent.

The extent of TC-related impacts is highly associated with TC size. The simulated TC circulation extents are compared to observations using the critical radius R_{34}, which is available in IBTrACS. As JTWC wind radii data provided in IBTrACS were only archived starting in 2001 and include many missing records, only 94 TCs out of 117 simulated TCs having available R_{34} data were used in this comparison. Larger frequency distribution of the simulated TC size sample indicates more data points compared to observations (Figure 2c). This is attributed to the generally higher intensity values simulated by WRF compared to observations (Figures 2a and 2b), which suggests that there are more maximum wind speed values above 34 kts, and hence more corresponding R_{34} values from the WRF simulations. This intensity attribute also leads to considerably larger size values in CTR compared to OBS illustrated by the higher 75th percentile. For size values less than 200 km, there is a consistency between the two samples represented by the matching 25th and 50th percentiles.

A further comparison of the impact for 34-, 50-, and 64-kt winds is shown in Figure 3. Note that to be comparable, these wind impacts are only from subsets of simulated TCs having available R_{34}, R_{60}, R_{64} observations (i.e., 94, 65, and 52 TCs, respectively). The simplified wind impacts (WI_{34s}, WI_{50s}, and WI_{64s}—left and middle columns) are in good agreement between the observation (OBS) and the model (CTR). This demonstrates a good performance by WRF in capturing critical wind radii of landfalling TCs in Southeast Asia both over the ocean and over land in spite of higher frequencies of all wind radii over the northern Philippines and the northern South China Sea and lower frequencies of R_{50}, R_{64} along the coastlines from southern China to Vietnam.

The above comparisons suggest that the WRF model is capable of reproducing both physical characteristics as well as wind and rain impacts of the present-day SEAL-TCs. The assessment of changes in the future climates is done by comparing the PGW simulations with the baseline period (CTR). Especially, for further analysis of the wind impacts, we will use the realistic calculation instead of the simplified one. This is derives from the fact that surface winds tend to erode rapidly due to the increased friction over the land surface and the lack of heat and moisture fluxes from the ocean energy source (e.g., DeMaria et al., 2006; Hlywiak & Nolan, 2021; Hubert, 1955; Kaplan & Demaria, 1995; Powell, 1987). Thus, the simplified calculation of the wind impact is likely to overestimate the actual wind impacts compared to the realistic calculation, as demonstrated clearly in Figure 3.

10.1029/2022EF003118

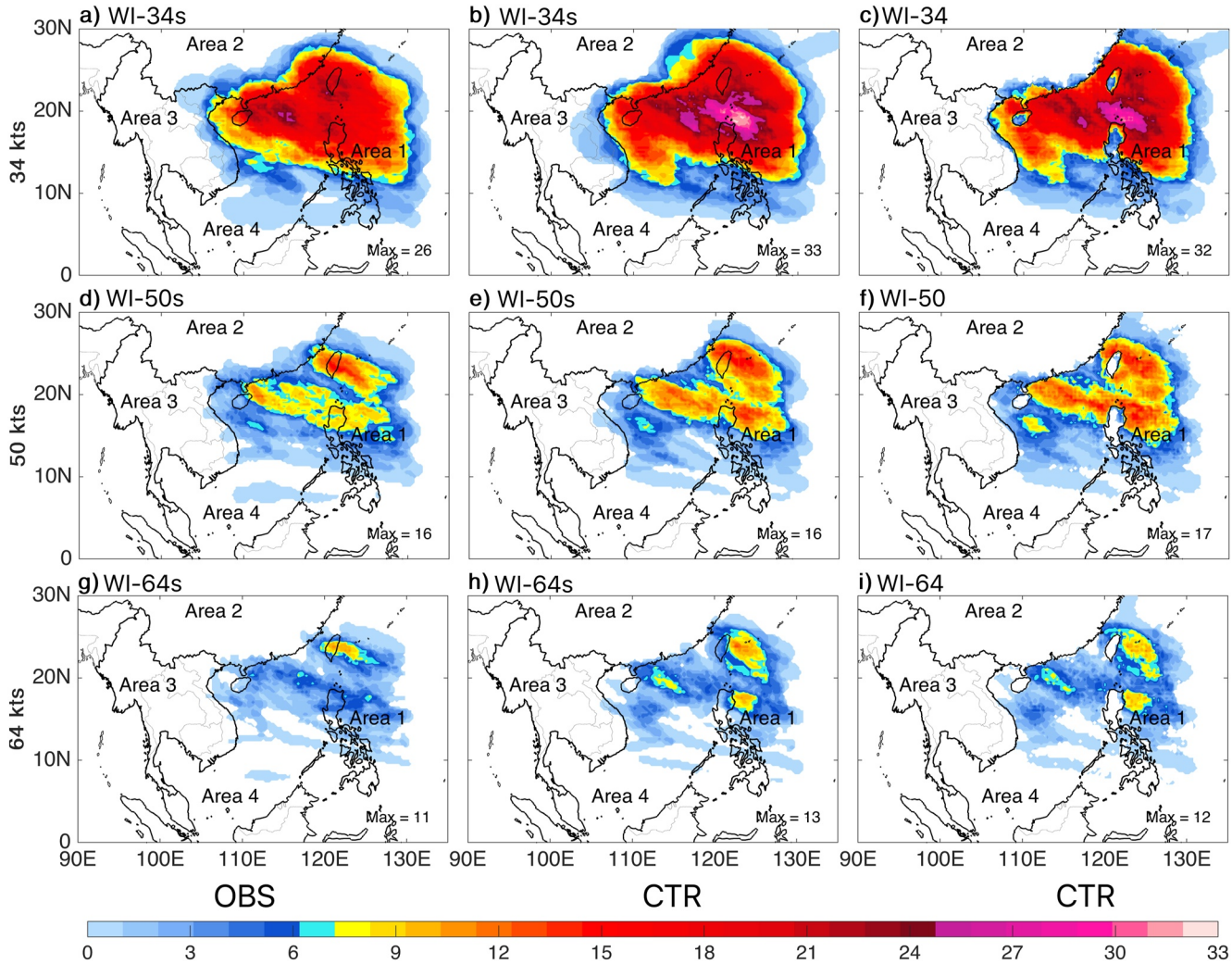

Figure 3. Comparison of wind impact at different critical wind speeds for OBS (simplified—left column) and CTR (simplified—middle column, and realistic—right column). See the description of simplified and realistic wind impact in Section 2.5.

3.2. TC Attributes Under Realistic Climate Change Scenarios

3.2.1. TC Intensity

The KS-test 2 results (Table S3 in Supporting Information S1) shows that the underlying cumulative distributions of *Pc* and V_{max} (not shown) in the 2050s and 2090s under the medium scenario, and in the 2090s under the high scenario are statistically different from the CTR distributions. This infers statistically significant changes in P_c and V_{max} under various levels of increased anthropogenic influence in the future. Detailed variations in TC intensity from current to future climates are exhibited in Figures 4a–4c. A distinct difference in 3-hourly P_c and V_{max} distribution occurs at the extreme intensities with the expansion of distributions (longer tails) in the future climates toward deeper P_c and higher V_{max} values compared to CTR (Figures 4a and 4b). This indicates that a larger proportion of the intense TCs is likely to occur more in the future which is consistent with previous studies (e.g., Knutson et al., 2015; Yamada et al., 2017). The largest changes are found for the 2090s period under the high-emission scenario (high2090s), with approximately 1% (9.25 hPa) decrease for the lower range of P_c, and 11% (14 kts) increase for the upper range of V_{max} (Table 2).

Our projections suggest that by the end of the 21st century under the high-emission scenario (radiative forcing of 7 Wm^{-2} by 2100) the most intense TCs might reach 170-kt winds and a central pressure of 860 hPa (increase 16% in V_{max} and decrease 4.5% in P_c compared to CTR) (e.g., Figure 5). These strongest intensity values generally agree with the upper limits (166 kts, 857 hPa, increase 19% in V_{max} and decrease 2.3% in P_c compared to CTR)

10.1029/2022EF003118

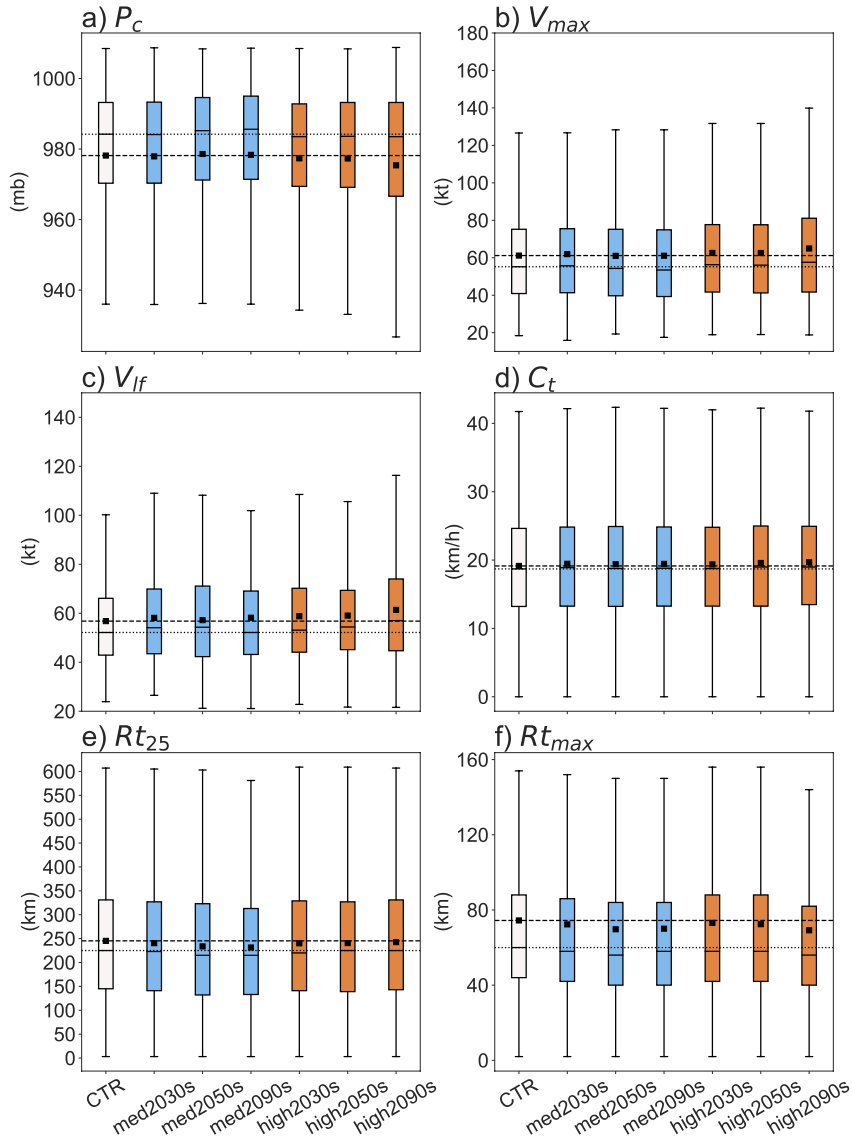

Figure 4. Box plots comparing the simulation for the present period (CTR, white) and future period simulations (blue and orange) for: (a) central pressure (P_c); (b) maximum intensity (V_{max}); (c) landfalling intensity (V_{lf}); (d) translation speed (C_t); (e) radius of 25-kt tangential winds (Rt_{25}); and (f) radius of maximum tangential winds (Rt_{max}) for 117 landfalling tropical cyclones. The black solid line and square in each box depict the median and mean values, respectively. For comparison purpose, the horizontal dotted- and dash-lines crossing through the median and mean of CTR are shown. The statistics are computed using a 3-hr output frequency.

for STYs in the WNP under the less extreme scenario—A1B (radiative forcing of 6.05 Wm^{-2} by 2100; Prather et al., 2013) in Tsuboki et al. (2015). Noted, however, that the study solely considered changes in SST.

There are notable changes of −0.28% (−2.78 hPa) and +6.18% (+3.78 kts) in the mean P_c and V_{max}, respectively in 2090s under the high-emission scenario compared to the current climate. These changes are significant at a 95% confidence level (Figures 4a and 4b, Table 2). At landfall, the average TC intensity increases 8% in the high2090s state compared to CTR (Table 2). The occurrence of more intense TCs making landfall in southern China by the end of the century was also found in Lok and Chan (2018) attributed to the presence of a warmer ocean and weaker vertical wind shear.

Two related metrics that provide additional detail on changes in TC overall wind energy and landfalling activity are the ACE index and the APDI. Previous studies suggest that for WNP or southern China landfalling TCs, ACE, and APDI will either decrease (Knutson et al., 2015) or not change (Lok & Chan, 2018) due to an offset between

Table 2
Differences in Tropical Cyclone Intensity Metrics Including Both Extreme and Mean Values Between the Present and Each Future State

	P_c		V_{max}		V_{lf}	
	Extreme (Δ) (mb)	Δ (%)	Extreme (Δ) (kt)	Δ (%)	Extreme (Δ) (kt)	Δ (%)
CTR	935.95		126.65		100.9	
med2030s	935.86 (−0.09)	−0.01	126.76 (+0.11)	0.09	109.54 (+8.64)	8.56
med2050s	936.10 (+0.15)	+0.02	128.45 (+1.8)	1.42	114.30 (+13.4)	13.28
med2090s	936.00 (+0.05)	+0.01	128.36 (+1.71)	1.35	107.92 (+7.02)	6.96
high2030s	934.30 (−1.65)	−0.18	131.70 (+5.05)	3.99	109.35 (+8.45)	8.37
high2050s	933.01 (−2.94)	−0.31	132.16 (+5.51)	4.35	105.65 (+4.75)	4.71
high2090s	926.70 (−9.25)	−0.99	140.20 (+13.55)	10.70	117.95 (+17.05)	16.90
	Mean (Δ) (mb)	Δ (%)	Mean (Δ) (kt)	Δ (%)	Mean (Δ) (kt)	Δ (%)
CTR	978.14		61.18		56.79	
med2030s	977.90 (−0.24)	−0.02	61.93 (+0.76)	+1.23	58.13 (+1.34)	+2.36
med2050s	978.59 (+0.45)	+0.05	61.03 (−0.14)	−0.23	57.19 (+0.39)	+0.69
med2090s	978.35 (+0.20)	+0.02	61.08 (−0.09)	−0.15	58.18 (+1.39)	+2.45
high2030s	977.35 (−0.79)	−0.08	62.59 (+1.41)	**+2.31****	58.78 (+1.99)	+3.50
high2050s	977.32 (−0.83)	**−0.08***	62.54 (+1.36)	**+2.23****	59.06 (+2.27)	+3.99
high2090s	975.37 (−2.78)	**−0.28****	64.96 (+3.78)	**+6.18****	61.36 (+4.57)	**+8.05****

Note. Statistically extreme values are defined using $1.5 \times IQR$ rule. Significant differences in mean values are tested by the Permutation test. Double (**) and single (*) asterisks accompanied with bold values indicate significant differences at 95% and 90% confident levels, respectively.

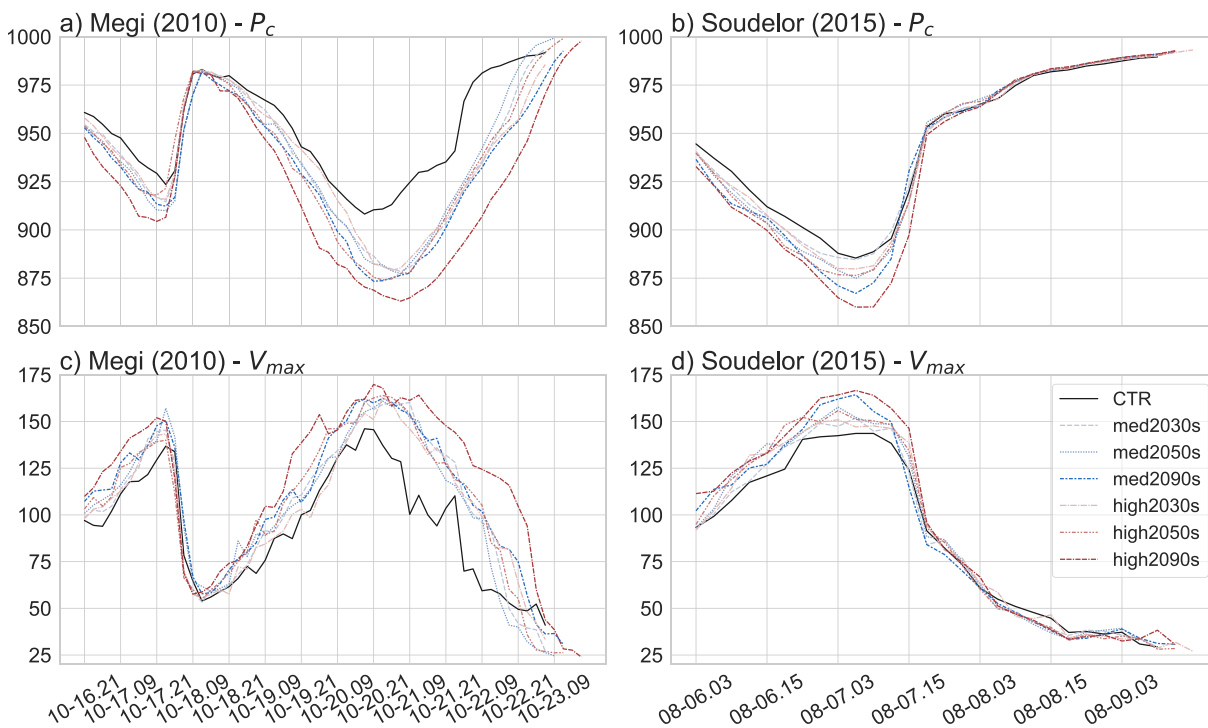

Figure 5. Time series (MM-DD.hh) of central pressure (*Pc*) and maximum wind (V_{max}) of the most intense tropical cyclones including: (a, c) Megi (2010); and (b, d) Soudelor (2015) in the CTR and future simulations.

Table 3
Accumulated Cyclone Energy (ACE), the Annual Power Dissipation Index (APDI), and the Integrated Kinetic Energy at Landfall (IKE_{lf}) for the Present Climate, Each Future Climate Scenario, and the Difference Between Them (Future—CTR)

	#Landfalls	ACE (kt^2)	ΔACE (%)	APDI ($\times 10^5$ kt^3)	ΔAPDI (%)	IKE_{lf} (TJ)	ΔIKE_{lf} (%)
CTR	200	933.2		513.9		31.5	
med2030s	196	936.4	+0.3	517.4	+0.7	30.0	−5.0
med2050s	197	921.9	−1.2	510.6	−0.6	28.3	−11.5
med2090s	192	920.2	−1.4	565.0	+10.0	28.3	−11.6
high2030s	193	950.4	+1.9	561.2	+8.4	31.5	−0.3
high2050s	191	970.7	+4.0	551.5	+6.7	33.2	+5.1
high2090s	195	1,061	+13.2	648.7	+24.5	33.3	+5.2

increased maximum winds but diminished TC frequency in these regions. Here, ACE is shown to increase by 13.2% by the end of the century under the high-emission scenario (Table 3), more than double the increasing rate of 5.6% of individual TC events projected in Wu et al. (2014) under the A1B scenario.

In the current climate, 117 TCs simulated using WRF made landfall for a total of 200 times due to some TCs making landfall more than once. In each future scenario, the track of each TC is altered because of the changed climate, and thus the number and location of landfall change for each TC instance (Table 3). APDI is a measure of landfall activity based on the sum of the cubic wind intensity at landfall and is thus dependent also on the number of landfalls. Despite the reduced number of TC landfalls compared to the present climate (Table 3), the ADPI is projected to increase in most future states. Strikingly, APDI increases by more than 24.5% by the end of the century under the high-emission scenario. However, the ADPI depends on just the single V_{max} value, changes in IKE_{lf}, which takes both the strength and distribution of the total TC wind field into account, better indicate land-falling TC potential impacts in Southeast Asia. Here, the aggregation of IKE_{lf} is projected to increase +5.2% in the high2090s climate state. The lower increasing rates in the 2050s and 2090s under the high-emission scenario along with a decrease in all other future states of IKE_{lf} compared to the APDI suggest a likelihood of a reduction in the horizontal scale of TCs which will be discussed in the next section.

3.2.2. TC Structure and Translation Speed

In general, there is a decreasing trend in both the inner-core size and whole circulation extent of TCs in the future (Figures 4e and 4f, Table 4). Significant decreases from 4.8% to 5.7% in the averaged TC outer size compared to the present climate are found in the mid and late century under the medium scenario. The TC inner-core size also diminishes at similar rates in the 2050s and 2090s under the medium scenario and up to 7% by the 2090s under the aggressive assumption of the high-emission scenario (Table 4).

Table 4
Changes in Mean Values of Tropical Cyclone (TC) Dynamical and Motion Parameters Between Current and Future Climates Including Inner-Core Size (Rtmax), the Whole Circulation Extent (Rt25), Translation Speed (Ct), and 3 Hourly Precipitation Within 100 km of the TC Center

	*Rt*25		*Rtmax*		Ct	
	Mean (km)	Δ (%)	Mean (km)	Δ (%)	Mean (km)	Δ (%)
CTR	245.30		74.42		19.14	
med2030s	240.42 (−4.88)	−1.99	72.33 (−2.10)	−2.82	19.46 (+0.32)	**+1.67***
med2050s	233.66 (−11.64)	**−4.75****	69.72 (−4.70)	**−6.32****	19.39 (+0.25)	+1.30
med2090s	231.33 (−13.97)	**−5.69****	70.06 (−4.36)	**−5.86****	19.45 (+0.31)	+1.61
high2030s	240.18 (−5.11)	−2.08	73.13 (−1.29)	−1.74	19.36 (+0.22)	+1.15
high2050s	240.62 (−4.67)	−1.91	72.44 (−1.99)	−2.6	19.58 (+0.44)	**+2.28****
high2090s	242.66 (−2.63)	−1.07	69.20 (−5.23)	**−7.02****	19.67 (+0.53)	**+2.77****

Note. Double (**) and single (*) asterisks accompanied with bold values indicate a significant difference (Future—CTR) at 95% and 90% confident levels, respectively tested by the Permutation test.

This finding disagrees with some previous studies that solely investigated the effects of increasing SST and found an increase in TC size (e.g., Sun et al., 2017; Yamada et al., 2017). On the other hand, our results are in agreement with the decrease in the circulation extent of general WNP TCs (Knutson et al., 2015) and the eyewall of extremely intense TCs approaching Japan (Kanada et al., 2013). Notably, changes in atmospheric conditions or sea ice are included in the two aforementioned studies. The integral role of atmospheric thermodynamic conditions including Ta, RH, and winds affects TC sizes in a different way than only considering SSTs. As the response in TC structure does not change linearly in response to the medium and high emission scenarios (Table 4, Figures 4e and 4f), it is likely that there are more complex interactions occurring as a result of changing several environmental parameters at the same time. The non-linear interactions among these environmental variables are likely affecting the response in TC structure because of how clouds and environmental patterns respond to the changes in these variables. There may also be other influencing factors such as inherent variabilities in the forcing data averaged from CMIP6 ensemble models. Details on how the combination of changed environmental conditions affect TC structure may shed some light on this and will be investigated in future work.

In contrast to the observed decrease in translation speed over land of global TCs in Kossin (2018), and of landfalling TCs in southern China in the WMO Regional Specialized Meteorological Center of Tokyo data set in Tran et al. (2022), the projections suggest that TCs will move faster in all future scenario combinations. By the 2030s, on average TCs will move approximately 1.67% faster under the medium scenario (significant at 90% confidence), and from 2.3% to 2.8% faster in the 2050s and 2090s under the high emission scenario (significant at 95% confidence) (Table 4, Figure 4d). Faster moving TCs result in a shorter exposure time to TC conditions but an increase in the TC right-of-track surface maximum wind speed (Shapiro, 1983), likely resulting in greater wind impacts in coastal areas (Parker et al., 2018). Furthermore, the risk of coastal inundation may increase as TCs speed up. Rego and Li (2009) conducted idealized experiments to assess the influence of TC parameters to coastal flooding over a wide and shallow shelf using the fully nonlinear Finite-Volume Coastal Ocean Model and found that an increase in forward motion can raise the maximum storm surge levels by as much as 40%. The underlying mechanism of the projected trend in TC translation speed are unknown at present and further investigation, beyond the scope of this paper, is needed to understand this result.

3.2.3. Tracking Pattern

As changes in TC attributes in the future were shown to be most robust in the 2090s, variations in TC exposure and physical impacts in the furthest future under both scenarios will be discussed in this section. Because the PGW framework is applied in this study without considering changes in TC genesis and frequency, possible departures in future spatial distributions of track density from the present climate are mainly caused by changes in the environmental steering flow and the environment—TC interaction. Under the medium scenario, there is a decrease in TC impacts in areas along southern China, while an increase is found in much of the Philippine archipelago, the northern part of the South China Sea including the sea adjacent to northern Vietnam (Figures 2e, 6a, and 6c). Under the high-emission scenario, there is a clear northwestward shift in the TC impact factor over time in the China southern coast from Guangxi to GuangDong (108°E to 117°E, hereafter, the southwestern coast of China), the northern half of Vietnam, the sea adjacent to central Vietnam, and decreases in time in the southern Philippines (Figures 2e, 6b, and 6d). Landfalling TCs along the southwestern coast of China and the northern half of Vietnam tend to penetrate hundreds of kilometers further inland and spread impacts to areas such as northern Laos, Thailand, or the Hunan province in China.

There are three possible reasons why the impacts extend further inland in Southeast Asia in the furthest future under the more aggressive scenario. First, because of climate change-induced increases in TC wind intensity (Figures 4a–4c, Table 2), it takes longer for TCs to spin down once they move over land and can travel longer distances. Second, it is physically possible that higher environmental moisture (e.g., Table 1) may feed convection for a longer period after TCs make landfall. This also helps to maintain the TC circulations against the effects of surface friction for longer (e.g., Deng & Ritchie, 2018). And third, the role of the environmental steering flow is critically important. Mittal et al. (2019) suggested that with a slight change in TC tracks, the steering flow is expected to dominate the Beta effect on TC trajectory. Here, an enhancement of the magnitude of environmental deep-layer mean (DLM) steering forces accompanied with a more favorable direction for TC landfall was found over northern Vietnam and southern China areas near Hainan Island by 2090 under the high-emission scenario (Figures 7a and 7c).

10.1029/2022EF003118

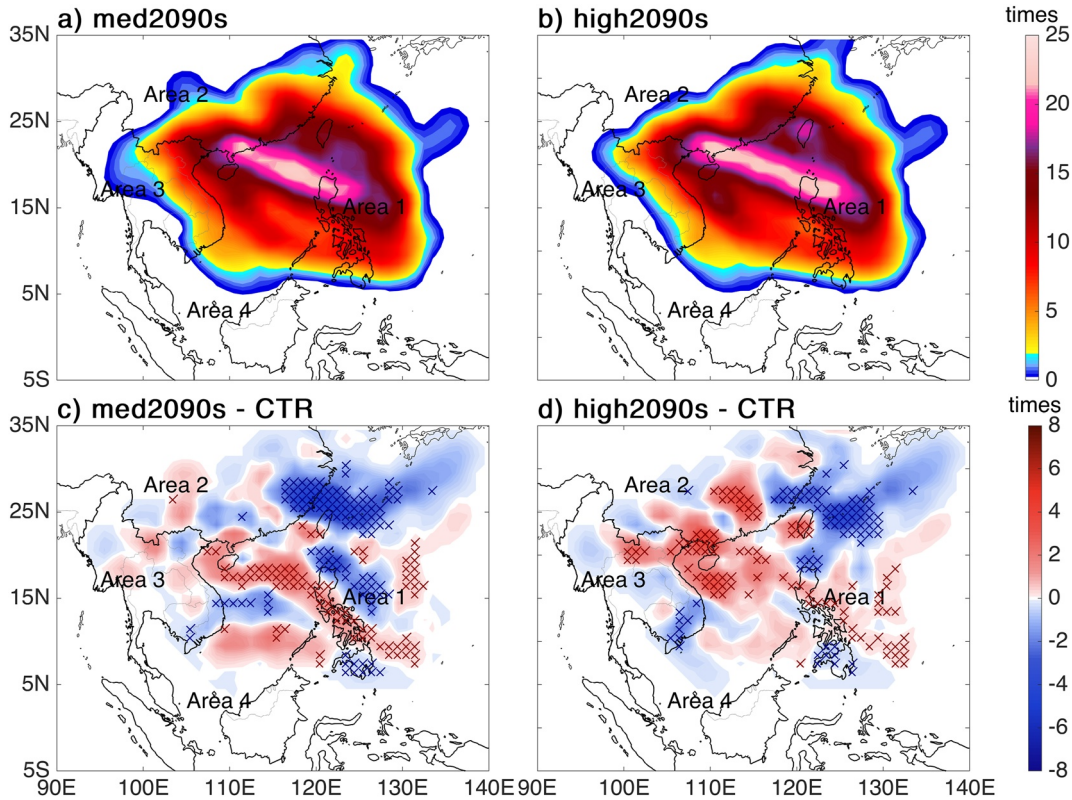

Figure 6. Track density in the 2090s under the: (a) medium; and (b) high-emission scenarios. Differences in track density between the 2090s future climate state and the present climate under the (c) medium; and (d) high-emission scenarios. In (c) and (d), shaded colors represent differences at each 1° spacing grid point, and the blue and red crosses indicate the Future-CTR difference comes from a distribution with the median smaller and greater than 0, respectively with 90% confidence level, tested by the Wilcoxon signed-rank test.

By contrast, the DLM steering flow over the China southern coast from Fujian to Zhejiang (117°E to 130°E, hereafter, the southeastern coast of China), the southern Philippines, and the southern half of Vietnam prohibits TCs from making landfall in these regions in the late century (Figures 6b, 6d, and 7c). Figure 8 illustrates the shift in latitude in tracks for some of the simulated TCs comparing the present climate and the med2090s and high2090s climate simulations. TCs that begin in both the South China Sea (Figures 8a and 8b) and the Philippines Sea (Figures 8c and 8d) are included. Note that no general shift in genesis location is included here, the shift in tracks occurs only due to the changes in the environmental steering flow and moisture. Under the high-emission scenario, several landfalling TCs, which either formed in the South China Sea (Figure 8b) or East Philippine Sea (Figure 8d) crossing southern or central Vietnam during the present climate, either dissipate near-shore or make landfall on the central coast of Vietnam at substantially higher latitudes due to unfavorable conditions from environmental steering flow toward the end of the 21st century (Figure 7c). Meanwhile, the northward shift in landfalling locations is smaller and inconsistent among those TCs under the medium scenario (Figures 8a and 8c).

By 2090s under the medium scenario, deviations in the direction of the DLM steering flow prevent TC landfalls in both Vietnam, China (Figure 7b). The increase in the median of the TC track density, hence, only occurs in the northern part of the South China Sea and in the Philippines (Figure 6c). These results here provide detailed changes in the TC track pattern in the 2090s under the medium and high-emission scenarios used in CMIP6 in Southeast Asia compared to the northward shift that has been found for the whole WNP under climate change scenarios used in CMIP3 and CMIP5 in previous studies (e.g., Kossin et al., 2016; Wu et al., 2014).

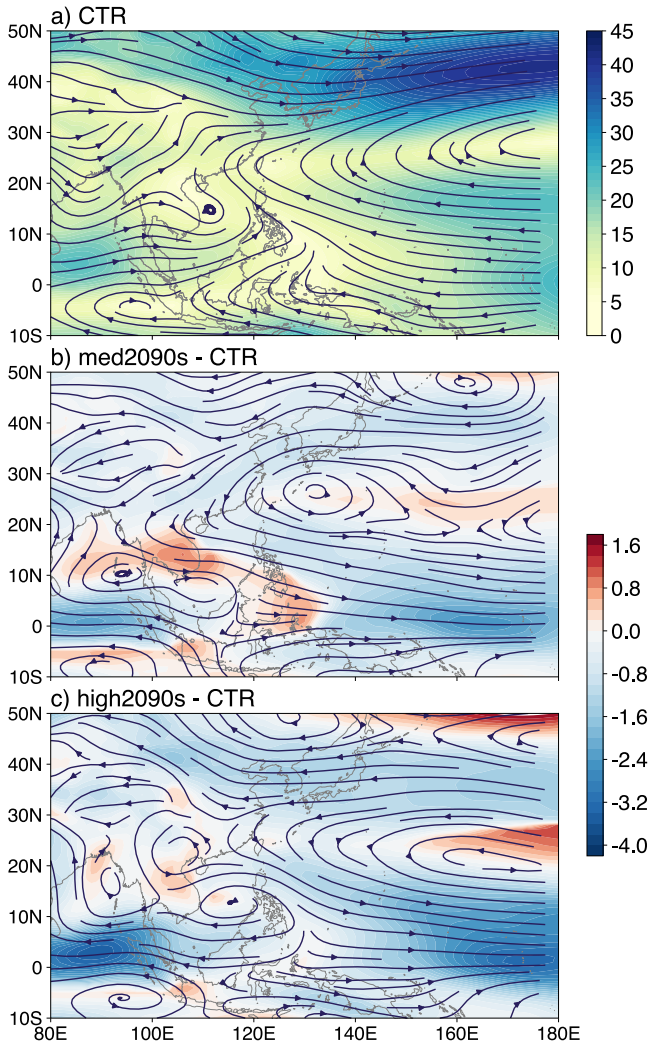

Figure 7. Averaged June-December deep-layer mean (DLM) (200–850 mb) steering flows for: (a) the present climate; (b) the difference between the 2090s under the medium scenario and current climates; and (c) the difference between the 2090s under the high-emission scenario and current climates. Shaded colors represent the magnitude of the DLM steering flow in (a), and magnitude of differences in (b) and (c). The unit of DLM steering flow magnitude is in kt.

3.3. TC Physical Impacts Over Southeast Asia in the Warming Futures

3.3.1. TC-Induced Wind Impacts

Fluctuations in projected TC-related wind impacts among future states are most prominent for winds of at least 34- and 50-kts by the 2090s (Figure 9). The northernmost locations of the Philippines, Taiwan, and coastal areas of southern China are most frequently impacted by at least 34- and 50-kt winds under both scenarios in the 2090s (Figures 9a, 9b, 9e and 9f). In comparison to the present climate, there is a consistent increase in TC wind impacts in areas in northern Vietnam, Hainan Island, Taiwan, and the northern Philippines under both scenarios but the spatial extent overland is broader under the high-emission scenario (Figures 9c, 9d, 9g and 9h). This is because of the further extension overland of TC tracks under the high-emission scenario (Figures 2e, 6b, and 6d) bringing wind impacts further inland in northern Vietnam, and even several locations in Laos and Thailand (Figures 9d and 9h). Under the medium scenario the increased track density is limited to the sea adjacent to northern Vietnam (Figures 2e, 6a, and 6c). The significant increase in median wind impacts at 90% confidence level is hence mostly found at several coastal locations in northern Vietnam and in Hainan Island (Figures 9c and 9g).

3.3.2. TC-Related Rain Impacts

Spatial patterns of total TC-induced precipitation normalized by TC in both the 2090s period and the baseline (CTR) over Southeast Asia, as well as the significant difference in their medians are shown in Figures 10a and 10c. Total rainfall increases over southern China, Taiwan, and the northern half of Vietnam, extending further inland over Laos and northern Thailand in the 2090s under the two scenarios (Figure 10a). However, the regions with significant median difference is patchy with a similar trend for both scenarios (Figure 10c). Generally, TC rainfall decreases in China, and increases in the northern regions of Laos, Thailand, and some locations in Myanmar. Although, these changes only cover small, isolated areas, mostly far inland from the coast, they are statistically significant (Figure 10c). It would be worth exploring this result further in future work with other experimental setups to evaluate how physically robust these results are.

Intense rain days, which are defined as days satisfying the threshold of exceeding 50 mm/day, can be a source of TC-induced flooding. Intense rain days most frequently occur in the coastal areas of Southeast Asia (Figure 10b). In the 2090s under both scenarios, intense rain days tend to appear less frequently in southern Vietnam, while impacted areas in northern Vietnam and along the southern China coast extend further inland along with an increase in frequency, especially in the 2090s, under the high-emission scenario. Figure 10d shows locations where there is a significant difference in the median of the frequency of intense rain days between future climate states in the 2090s and the present climate. Significant changes are concentrated much closer to the coastline compared with total rainfall (Figures 10c and 10d). In particular, more intense rain days are projected to occur on both sides of the border between northern Vietnam and southern China, while some areas in central Vietnam, southern China east of 114°E tends to be less frequently influenced by TC intense rain days in the future scenarios.

4. Conclusion and Discussion

This largest-to-date PGW study has identified potential changes in the climatology of both landfalling attributes and physical impacts of TCs in Southeast Asia. We impose a full set of atmospheric and oceanic perturbations based on the most recent climate change scenarios. The model was capable of reasonably simulating

10.1029/2022EF003118

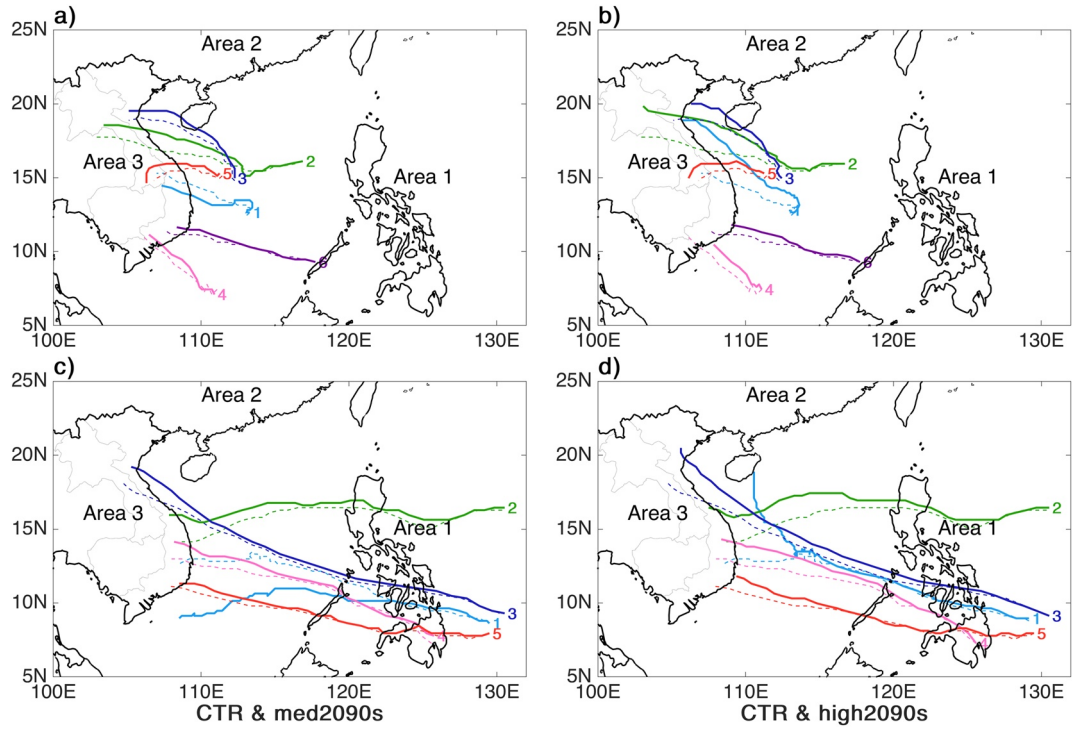

Figure 8. A shift in spatial distributions of tropical cyclones (TCs) making landfall in the southern and central Vietnam from the present climate to the end of the 21st century under the: (a, c) medium; and (b, d) high-emission scenarios. Top panels (a, b): TCs forming in the South China Sea, Bottom panels (c, d): TCs forming in the Philippine Sea. For the sake of clarity, different TC tracks are labeled with numbers and colors, the solid lines indicate the future-period simulations and the dashed lines indicate the baseline simulations (CTR).

characteristics of the SEAL-TCs in the last two decades despite of an underestimation of the strongest wind. The current climate results suggest reasonable confidence in investigating the response of present SEAL-TCs to climate change scenarios in the early, mid, and late 21st century.

The proportion of intense TCs increases in the future is in agreement with previous studies. It may be possible for TCs to attain maximum wind speeds of 170 kt and a central pressure of 860 hPa by 2090 under the high-emission scenario. Among available projections in the WNP, which are rescaled to be consistent with a mean global warming of 2°C, the 10th and 90th percentiles of TC intensity increase are 2% and 9%, respectively (Cha et al., 2020). Our results under the high-emission scenario, which projects a 4.1°C warming in mean global temperature, show that the average and landfalling intensities are projected to increase by 6% and 8% by 2090. As a result, ACE and APDI can increase up to 13.2% and 25%, respectively, if excluding potential changes in TC landfalling frequency. In term of TC structure, both inner-core and outer-core sizes are projected to be more compact in the future, supporting the finding for the WNP basin in Knutson et al. (2015). The combination of the increased intensity and decreased size leads to a smaller increase of +5.2% in IKE at landfall, which represents the damage potential of TCs at landfall.

No robust changing signal in the translation speed of WNP TCs was found in the available literature (e.g., Kim et al., 2014; Wu et al., 2014). Our projections suggest a slight increase by 1.7%–2.8% in TC motion in some specific future climate states including the 2030s under the medium scenario, and the 2050s and 2090s under the high-emission scenario. Subsequently, there may be greater coastal risks from enhanced TC surface winds and inundation due to the associated increase in maximum storm surge as TCs move faster.

The TC track density significantly enhances in the 2050s and 2090s periods under the high-emission scenario in the northern areas of Southeast Asia and southwestern China, while lessens in the southern areas of Southeast Asia and southeastern China. In the late 21st century under the high-emission scenario, TCs making landfall tend to dissipate earlier in southern and central Vietnam, but travel further inland in northern Vietnam and southwestern China. Regardless of potential variations in TC frequency and TC genesis location, these changes in TC

10.1029/2022EF003118

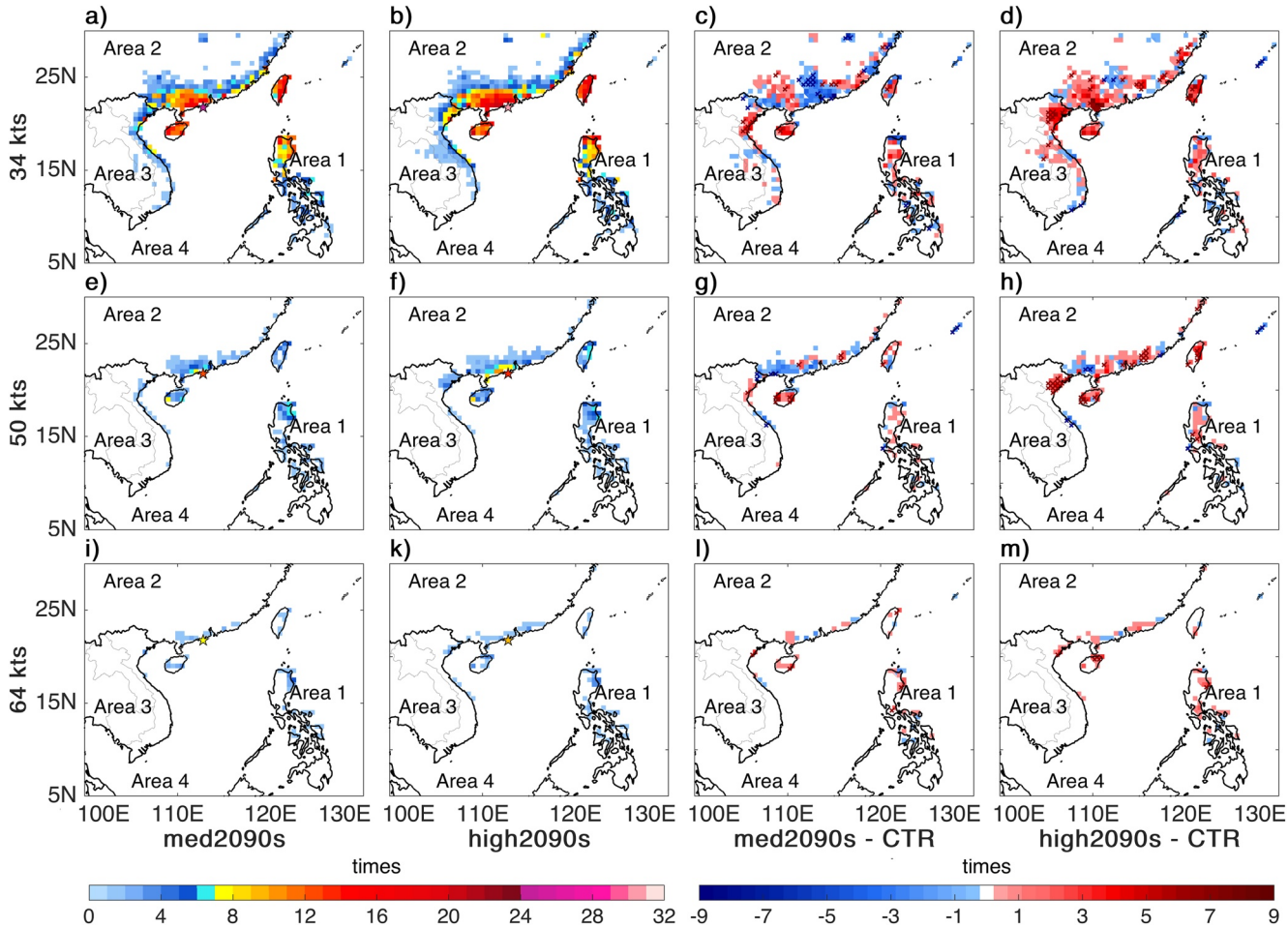

Figure 9. Impacted frequency of at least 34-, 50-, 64-kt winds in the 2090s under the: (a, e, i) medium; and (b, f, k) high-emission scenarios. The corresponding differences of each wind categories in the 2090s under the: (c, g, l) medium; and (d, h, m) high-emission scenarios from current climate. Blue and red shades in (c, d, g, h, l, m) represent differences at each grid point of 0.5° resolution. The blue and red crosses denote a 90% confidence level using the Wilcoxon rank-sum test.

trajectories in future climates may result from the increases in TC intensity and environmental moisture, which result in a longer spin down time over land, as well as the changes of the background steering flow.

The concurrent changes in TC attributes including intensity, structure, precipitation, translation speed, and tracks modulate TC related wind and rain impacts in Southeast Asia in future climates. By the end of the century, TC rain and wind impacts decrease in southeastern China and the southern areas of Southeast Asia. By contrast, TC threats from winds and rainfall are projected to increase in southwestern China and other northern regions of Southeast Asia, including areas further inland under the high-emission scenario requiring a thorough preparedness and management of catastrophic disasters for those areas in the future.

It is important to note that the future projections could be affected by the following factors. First, the 10-year average FNL and CMIP6 ensemble chosen to represent the current and future climates driving the downscaling simulations may not be long enough to smooth inherent decadal and multidecadal variabilities in some coupled climate models (e.g., Emanuel et al., 2008; Parker et al., 2018). In this study, however, an ensemble mean was used to mitigate this effect to some extent. Second, the WRF modeling system used to downscale CMIP6-perturbed reanalysis data did not include ocean coupling, therefore the TC-induced "cold wake" in the SST field, which has important negative feedback on TC intensity (e.g., Bender & Ginis, 2000; Knutson et al., 2001; Lin et al., 2013) was not considered. In addition, although simulations were run with a fine mesh of 2 km spatial resolution, the WRF model was found to underestimate the strongest TC winds. Therefore, the results of the responses of TC intensity to global warming might be underestimated. Lastly, radiatively-forced changes in TC genesis frequency and location were held constant throughout the future states in this study, which is also the main

10.1029/2022EF003118

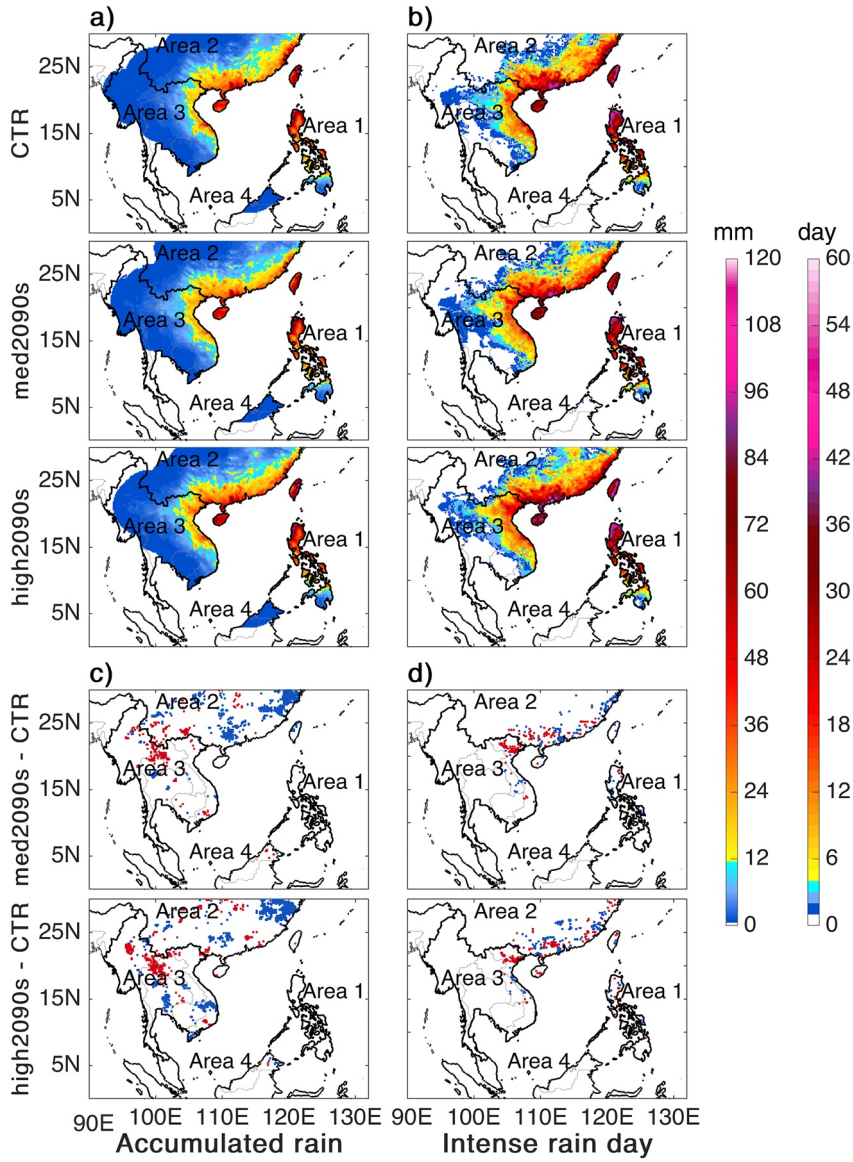

Figure 10. (a) Accumulated rainfall normalized by tropical cyclone (TC) (unit in mm) in the present, and 2090s under the medium and high-emission scenarios. (c) Significant difference for the median of accumulated rainfall normalized by TC at each grid point of 18 km between each future state under the medium and high-emission scenarios and the control run, using the Wilcoxon rank-sum test. (b, d) are similar to (a, c), respectively but for Intense rain day (unit in day). The left and right colorbars are for Accumulated rainfall and Intense rain day, respectively. Red (blue) shading in (c, d) denotes increasing (decreasing) trends at a 90% confidence level.

caveat of the PGW framework (Gutmann et al., 2018). While the TC frequency strongly associates with the TC-related impacts, their projections in future climates are largely uncertain (e.g., Cha et al., 2020; Knutson et al., 2020; Sobel et al., 2021). Naturally, no TC impacts occur if no TC forms, however if there is an increase in TC frequency, that could lead to an increase in TC impacts with related growth in consequences. Moreover, shifts in TC genesis locations under climate change scenarios along with changes in large-scale steering flows could lead to changes in TC track density and cause changes to the exposure sites. Future research taking into account the factors mentioned above will further enhance the confidence for TC projections.

In conclusion, the results presented have provided improved knowledge of some potential projections and more importantly the physical interpretations of their attributes and physical impacts in Southeast Asia. The patterns of TC landfall and related impacts in the future highlight increasingly higher threats posed by TCs to people and

property in Southeast Asia. Further studies on TC risks in the region are essential to assist governments, policy-makers, stakeholders, and communities in this region to better manage and adapt to future change of TC hazards.

Data Availability Statement

This research was undertaken with the assistance of resources and services from the National Computational Infrastructure (NCI), which is supported by the Australian Government. The CMIP6 data set used in this study is available at https://esgf-node.llnl.gov/search/cmip6/. Users should select the variables as psl, tos, hur, ta, ua, and va which stand for sea level pressure, sea surface temperature, relative humidity, air temperature, eastward wind and northward wind, respectively; the frequency as monthly; select Experiment ID as historical, ssp245, and ssp370; select CMIP6 models that found in this study (See Table S1 in Supporting Information S1 for a brief description on the used CMIP6 models); and then download the .nc files that appear as search outputs. The 50 million Natural Earth Coastline data sets version 4.1.0 can be downloaded from https://www.naturalearthdata.com/downloads/. The ETOPO1 1 arc-minute global relief model (NOAA, 2009) is available at 10.7289/V5C8276M; IBTrACS data version 4 (Knapp et al., 2018) provided by NOAA National Centers for Environmental Information can be accessed at https://www.ncdc.noaa.gov/ibtracs/index.php?name=ib-v4-access. The TRMM (TMPA) Rainfall Estimate L3 3 hr 0.25 × 0.25° V7 data set (Greenbelt, 2011) is available at https://doi.org/10.5067/TRMM/TMPA/3H/7.

Acknowledgments
This article is based on part of the first author's PhD thesis, which was supported by the Australian Government Endeavour Leadership Program (PhD scholarship - 6614—2018) and a UNSW scholarship (Int'l MOUs PTFS—RSRE7073). The authors would like to thank the editor and two reviewers for the constructive feedback for improving the manuscript.

References

Au-Yeung, A. Y. M., & Chan, J. C. L. (2012). Potential use of a regional climate model in seasonal tropical cyclone activity predictions in the western North Pacific. *Climate Dynamics*, *39*(3), 783–794. https://doi.org/10.1007/s00382-011-1268-x

Bender, M. A., & Ginis, I. (2000). Real-case simulations of hurricane–ocean interaction using a high-resolution coupled model: Effects on hurricane intensity. *Monthly Weather Review*, *128*(4), 917–946. https://doi.org/10.1175/1520-0493(2000)128⟨0917:Rcsoho⟩2.0.Co;2

Bretherton, C. S., & Park, S. (2009). A new moist turbulence parameterization in the community atmosphere model. *Journal of Climate*, *22*(12), 3422–3448. https://doi.org/10.1175/2008jcli2556.1

Camargo, S. J. (2013). Global and regional aspects of tropical cyclone activity in the CMIP5 models. *Journal of Climate*, *26*(24), 9880–9902. https://doi.org/10.1175/jcli-d-12-00549.1

Castro, C. L., Chang, H.-I., Dominguez, F., Carrillo, C., Schemm, J.-K., & Henry Juang, H.-M. (2012). Can a regional climate model improve the ability to forecast the North American monsoon? *Journal of Climate*, *25*(23), 8212–8237. https://doi.org/10.1175/jcli-d-11-00441.1

Cha, E. J., Knutson, T. R., Lee, T.-C., Ying, M., & Nakaegawa, T. (2020). Third assessment on impacts of climate change on tropical cyclones in the typhoon committee region—Part II: Future projections. *Tropical Cyclone Research and Review*, *9*(2), 75–86. https://doi.org/10.1016/j.tcrr.2020.04.005

Chang, L. T. C., Cheung, K. K. W., & McAneney, J. (2013). Case study of TRMM satellite rainfall estimation for landfalling tropical cyclones: Issues and challenges. *Tropical Cyclone Research and Review*, *2*(2), 109–123. https://doi.org/10.6057/2013TCRR02.04

Chen, A., Emanuel, K. A., Chen, D., Lin, C., & Zhang, F. (2020). Rising future tropical cyclone-induced extreme winds in the Mekong River Basin. *Science Bulletin*, *65*(5), 419–424. https://doi.org/10.1016/j.scib.2019.11.022

Dare, R. A., Davidson, N. E., & McBride, J. L. (2012). Tropical cyclone contribution to rainfall over Australia. *Monthly Weather Review*, *140*(11), 3606–3619. https://doi.org/10.1175/mwr-d-11-00340.1

Davis, C., Wang, W., Chen, S. S., Chen, Y., Corbosiero, K., DeMaria, M., et al. (2008). Prediction of landfalling hurricanes with the advanced hurricane WRF model. *Monthly Weather Review*, *136*(6), 1990–2005. https://doi.org/10.1175/2007mwr2085.1

DeMaria, M., Knaff, J. A., & Kaplan, J. (2006). On the decay of tropical cyclone winds crossing narrow landmasses. *Journal of Applied Meteorology and Climatology*, *45*(3), 491–499. https://doi.org/10.1175/jam2351.1

Deng, D., & Ritchie, E. A. (2018). Rainfall characteristics of recurving tropical cyclones over the western north Pacific. *Journal of Climate*, *31*(2), 575–592. https://doi.org/10.1175/jcli-d-17-0415.1

Done, J. M., Bruyère, C. L., Ge, M., & Jaye, A. (2014). Internal variability of North Atlantic tropical cyclones. *Journal of Geophysical Research: Atmospheres*, *119*(11), 6506–6519. https://doi.org/10.1002/2014jd021542

Dudhia, J. (1989). Numerical study of convection observed during the winter monsoon experiment using a mesoscale two-dimensional model. *Journal of the Atmospheric Sciences*, *46*(20), 3077–3107. https://doi.org/10.1175/1520-0469(1989)046⟨3077:Nsocod⟩2.0.Co;2

Emanuel, K. (1999). Thermodynamic control of hurricane intensity. *Nature*, *401*(6754), 665–669. https://doi.org/10.1038/44326

Emanuel, K. (2021). Response of global tropical cyclone activity to increasing CO_2: Results from downscaling CMIP6 models. *Journal of Climate*, *34*(1), 57–70. https://doi.org/10.1175/jcli-d-20-0367.1

Emanuel, K., & Sobel, A. (2013). Response of tropical sea surface temperature, precipitation, and tropical cyclone-related variables to changes in global and local forcing. *Journal of Advances in Modeling Earth Systems*, *5*(2), 447–458. https://doi.org/10.1002/jame.20032

Emanuel, K., Sundararajan, R., & Williams, J. (2008). Hurricanes and global warming: Results from downscaling IPCC AR4 simulations. *Bulletin of the American Meteorological Society*, *89*(3), 347–368. https://doi.org/10.1175/bams-89-3-347

Englehart, P. J., & Douglas, A. V. (2001). The role of eastern North Pacific tropical storms in the rainfall climatology of western Mexico. *International Journal of Climatology*, *21*(11), 1357–1370. https://doi.org/10.1002/joc.637

Feser, F., & Storch, H. V. (2008). A dynamical downscaling case study for typhoons in Southeast Asia using a regional climate model. *Monthly Weather Review*, *136*(5), 1806–1815. https://doi.org/10.1175/2007mwr2207.1

Gentry, M. S., & Lackmann, G. M. (2010). Sensitivity of simulated tropical cyclone structure and intensity to horizontal resolution. *Monthly Weather Review*, *138*(3), 688–704. https://doi.org/10.1175/2009mwr2976.1

Greenbelt, M. (2011). Tropical rainfall measuring mission (TRMM TMPA) rainfall estimate L3 3 hour 0.25 degree × 0.25 degree v7 [Dataset]. Goddard Earth Sciences Data and Information Services Center (GES DISC). http://dx.doi.org/10.5067/TRMM/TMPA/3H/7

Gutmann, E. D., Rasmussen, R. M., Liu, C., Ikeda, K., Bruyere, C. L., Done, J. M., et al. (2018). Changes in hurricanes from a 13-yr convection-permitting pseudo–global warming simulation. *Journal of Climate*, *31*(9), 3643–3657. https://doi.org/10.1175/jcli-d-17-0391.1

Hart, R. E., & Evans, J. L. (2001). A climatology of the extratropical transition of Atlantic tropical cyclones. *Journal of Climate*, *14*(4), 546–564. https://doi.org/10.1175/1520-0442(2001)014⟨0546:Acotet⟩2.0.Co;2

Hausfather, Z., & Peters, G. (2020). Emissions—The 'business as usual' story is misleading. *Nature*, *577*(7792), 618–620. https://doi.org/10.1038/d41586-020-00177-3

Heming, J. T. (2017). Tropical cyclone tracking and verification techniques for met office numerical weather prediction models. *Meteorological Applications*, *24*(1), 1–8. https://doi.org/10.1002/met.1599

Hill, K. A., & Lackmann, G. M. (2011). The impact of future climate change on tc intensity and structure: A downscaling approach. *Journal of Climate*, *24*(17), 4644–4661. https://doi.org/10.1175/2011jcli3761.1

Hlywiak, J., & Nolan, D. S. (2021). The response of the near-surface tropical cyclone wind field to inland surface roughness length and soil moisture content during and after landfall. *Journal of the Atmospheric Sciences*, *78*(3), 983–1000. https://doi.org/10.1175/jas-d-20-0211.1

Holland, G. J. (1997). The maximum potential intensity of tropical cyclones. *Journal of the Atmospheric Sciences*, *54*(21), 2519–2541. https://doi.org/10.1175/1520-0469(1997)054⟨2519:Tmpiot⟩2.0.Co;2

Hubert, L. F. (1955). Frictional filling of hurricanes. *Bulletin of the American Meteorological Society*, *36*(9), 440–445. https://doi.org/10.1175/1520-0477-36.9.440

Jiang, H., Halverson, J. B., Simpson, J., & Zipser, E. J. (2008). Hurricane "rainfall potential" derived from satellite observations aids overland rainfall prediction. *Journal of Applied Meteorology and Climatology*, *47*(4), 944–959. https://doi.org/10.1175/2007jamc1619.1

Kain, J. S. (2004). The Kain–Fritsch convective parameterization: An update. *Journal of Applied Meteorology*, *43*(1), 170–181. https://doi.org/10.1175/1520-0450(2004)043⟨0170:tkcpau⟩2.0.co;2

Kanada, S., Wada, A., & Sugi, M. (2013). Future changes in structures of extremely intense tropical cyclones using a 2-km mesh nonhydrostatic model. *Journal of Climate*, *26*(24), 9986–10005. https://doi.org/10.1175/jcli-d-12-00477.1

Kaplan, J., & Demaria, M. (1995). A simple empirical model for predicting the decay of tropical cyclone winds after landfall. *Journal of Applied Meteorology*, *34*(11), 2499–2512. https://doi.org/10.1175/1520-0450(1995)034⟨2499:asemfp⟩2.0.co;2

Khouakhi, A., Villarini, G., & Vecchi, G. A. (2017). Contribution of tropical cyclones to rainfall at the global scale. *Journal of Climate*, *30*(1), 359–372. https://doi.org/10.1175/jcli-d-16-0298.1

Kilroy, G., Smith, R. K., & Montgomery, M. T. (2016). Why do model tropical cyclones grow progressively in size and decay in intensity after reaching maturity? *Journal of the Atmospheric Sciences*, *73*(2), 487–503. https://doi.org/10.1175/jas-d-15-0157.1

Kim, H.-S., Vecchi, G. A., Knutson, T. R., Anderson, W. G., Delworth, T. L., Rosati, A., et al. (2014). Tropical cyclone simulation and response to CO_2 doubling in the GFDL CM2.5 high-resolution coupled climate model. *Journal of Climate*, *27*(21), 8034–8054. https://doi.org/10.1175/jcli-d-13-00475.1

Knapp, K. R., Diamond, H. J., Kossin, J. P., Kruk, M. C., & Schreck, C. J. I. (2018). International best track archive for climate stewardship (IBTRACS) project, version 4 [Dataset]. NOAA National Centers for Environmental Information. http://dx.doi.org/10.25921/82ty-9e16

Knutson, T. R., Camargo, S. J., Chan, J. C. L., Emanuel, K., Ho, C.-H., Kossin, J., et al. (2020). Tropical cyclones and climate change assessment: Part ii: Projected response to anthropogenic warming. *Bulletin of the American Meteorological Society*, *101*(3), E303–E322. https://doi.org/10.1175/bams-d-18-0194.1

Knutson, T. R., Sirutis, J. J., Vecchi, G. A., Garner, S., Zhao, M., Kim, H.-S., et al. (2013). Dynamical downscaling projections of twenty-first-century Atlantic hurricane activity: CMIP3 and CMIP5 model-based scenarios. *Journal of Climate*, *26*(17), 6591–6617. https://doi.org/10.1175/jcli-d-12-00539.1

Knutson, T. R., Sirutis, J. J., Zhao, M., Tuleya, R. E., Bender, M., Vecchi, G. A., et al. (2015). Global projections of intense tropical cyclone activity for the late twenty-first century from dynamical downscaling of CMIP5/RCP4.5 scenarios. *Journal of Climate*, *28*(18), 7203–7224. https://doi.org/10.1175/jcli-d-15-0129.1

Knutson, T. R., Tuleya, R. E., Shen, W., & Ginis, I. (2001). Impact of CO_2-induced warming on hurricane intensities as simulated in a hurricane model with ocean coupling. *Journal of Climate*, *14*(11), 2458–2468. https://doi.org/10.1175/1520-0442(2001)014⟨2458:Iociwo⟩2.0.Co;2

Korty, R. L., Emanuel, K. A., Huber, M., & Zamora, R. A. (2017). Tropical cyclones downscaled from simulations with very high carbon dioxide levels. *Journal of Climate*, *30*(2), 649–667. https://doi.org/10.1175/jcli-d-16-0256.1

Kossin, J. P. (2018). A global slowdown of tropical-cyclone translation speed. *Nature*, *558*(7708), 104–107. https://doi.org/10.1038/s41586-018-0158-3

Kossin, J. P., Emanuel, K. A., & Camargo, S. J. (2016). Past and projected changes in western north Pacific tropical cyclone exposure. *Journal of Climate*, *29*(16), 5725–5739. https://doi.org/10.1175/jcli-d-16-0076.1

Kreussler, P., Caron, L.-P., Wild, S., Loosveldt Tomas, S., Chauvin, F., Moine, M.-P., et al. (2021). Tropical cyclone integrated kinetic energy in an ensemble of HighResMIP simulations. *Geophysical Research Letters*, *48*(5), e2020GL090963. https://doi.org/10.1029/2020GL090963

Lackmann, G. M. (2015). Hurricane sandy before 1900 and after 2100. *Bulletin of the American Meteorological Society*, *96*(4), 547–560. https://doi.org/10.1175/bams-d-14-00123.1

Leary, L. A., & Ritchie, E. A. (2009). Lightning flash rates as an indicator of tropical cyclone Genesis in the eastern north Pacific. *Monthly Weather Review*, *137*(10), 3456–3470. https://doi.org/10.1175/2009mwr2822.1

Lin, I.-I., Black, P., Price, J. F., Yang, C.-Y., Chen, S. S., Lien, C.-C., et al. (2013). An ocean coupling potential intensity index for tropical cyclones. *Geophysical Research Letters*, *40*(9), 1878–1882. https://doi.org/10.1002/grl.50091

Lind, P., Lindstedt, D., Kjellström, E., & Jones, C. (2016). Spatial and temporal characteristics of summer precipitation over central Europe in a suite of high-resolution climate models. *Journal of Climate*, *29*(10), 3501–3518. https://doi.org/10.1175/jcli-d-15-0463.1

Liu, K. S., & Chan, J. C. L. (2017). Variations in the power dissipation index in the East Asia region. *Climate Dynamics*, *48*(5), 1963–1985. https://doi.org/10.1007/s00382-016-3185-5

Lok, C. C. F., & Chan, J. C. L. (2018). Changes of tropical cyclone landfalls in south China throughout the twenty-first century. *Climate Dynamics*, *51*(7), 2467–2483. https://doi.org/10.1007/s00382-017-4023-0

Lynch, P., & Huang, X.-Y. (1992). Initialization of the HIRLAM model using a digital filter. *Monthly Weather Review*, *120*(6), 1019–1034. https://doi.org/10.1175/1520-0493(1992)120⟨1019:iothmu⟩2.0.co;2

Lynn, B. H., Healy, R., & Druyan, L. M. (2009). Investigation of Hurricane Katrina characteristics for future, warmer climates. *Climate Research*, *39*(1), 75–86. https://doi.org/10.3354/cr00801

Massey, F. J. (1951). The Kolmogorov-Smirnov test for goodness of fit. *Journal of the American Statistical Association*, *46*(253), 68–78. https://doi.org/10.1080/01621459.1951.10500769

Meinshausen, M., Nicholls, Z. R. J., Lewis, J., Gidden, M. J., Vogel, E., Freund, M., et al. (2020). The shared socio-economic pathway (SSP) greenhouse gas concentrations and their extensions to 2500. *Geoscientific Model Development*, *13*(8), 3571–3605. https://doi.org/10.5194/gmd-13-3571-2020

Mittal, R., Tewari, M., Radhakrishnan, C., Ray, P., Singh, T., & Nickerson, A. (2019). Response of tropical cyclone Phailin (2013) in the Bay of Bengal to climate perturbations. *Climate Dynamics*, *53*(3–4), 2013–2030. https://doi.org/10.1007/s00382-019-04761-w

Mlawer, E. J., Taubman, S. J., Brown, P. D., Iacono, M. J., & Clough, S. A. (1997). Radiative transfer for inhomogeneous atmospheres: RRTM, a validated correlated-k model for the longwave. *Journal of Geophysical Research*, *102*(D14), 16663–16682. https://doi.org/10.1029/97jd00237

Morrison, H., Thompson, G., & Tatarskii, V. (2009). Impact of cloud microphysics on the development of trailing stratiform precipitation in a simulated squall line: Comparison of one- and two-moment schemes. *Monthly Weather Review*, *137*(3), 991–1007. https://doi.org/10.1175/2008mwr2556.1

Nakamura, J., Camargo, S. J., Sobel, A. H., Henderson, N., Emanuel, K. A., Kumar, A., et al. (2017). Western north Pacific tropical cyclone model tracks in present and future climates. *Journal of Geophysical Research: Atmospheres*, *122*(18), 9721–9744. https://doi.org/10.1002/2017jd027007

Nakamura, R., Shibayama, T., Esteban, M., & Iwamoto, T. (2016). Future typhoon and storm surges under different global warming scenarios: Case study of typhoon Haiyan (2013). *Natural Hazards*, *82*(3), 1645–1681. https://doi.org/10.1007/s11069-016-2259-3

Niu, Y., Touma, D., Ting, M., Camargo, S. J., & Chen, R. (2022). Assessing heavy precipitation risk associated with tropical cyclones in China. *Journal of Applied Meteorology and Climatology*, *61*(5), 577–591. https://doi.org/10.1175/jamc-d-21-0166.1

NOAA, NGDC. (2009). ETOPO1 1 arc-minute global relief model [Dataset]. NOAA. http://dx.doi.org/10.7289/V5C8276M

Omrani, H., Drobinski, P., & Dubos, T. (2012). Spectral nudging in regional climate modelling: How strongly should we nudge? *Quarterly Journal of the Royal Meteorological Society*, *138*(668), 1808–1813. https://doi.org/10.1002/qj.1894

O'Neill, B. C., Tebaldi, C., Van Vuuren, D. P., Eyring, V., Friedlingstein, P., Hurtt, G., et al. (2016). The scenario model intercomparison project (ScenarioMIP) for CMIP6. *Geoscientific Model Development*, *9*(9), 3461–3482. https://doi.org/10.5194/gmd-9-3461-2016

Parker, C. L., Bruyère, C. L., Mooney, P. A., & Lynch, A. H. (2018). The response of land-falling tropical cyclone characteristics to projected climate change in northeast Australia. *Climate Dynamics*, *51*(9), 3467–3485. https://doi.org/10.1007/s00382-018-4091-9

Peckham, S. E., Smirnova, T. G., Benjamin, S. G., Brown, J. M., & Kenyon, J. S. (2015). Implementation of a digital filter initialization in the WRF model and its application in the Rapid Refresh. *Monthly Weather Review*, *144*(1), 99–106. https://doi.org/10.1175/mwr-d-15-0219.1

Phipson, B., & Smyth, G. K. (2010). Permutation p-values should never be zero: Calculating exact p-values when permutations are randomly drawn. *Statistical Applications in Genetics and Molecular Biology*, *9*(1), 1–16. https://doi.org/10.2202/1544-6115.1585

Powell, M. (1987). Changes in the low-level kinematic and thermodynamic structure of Hurricane Alicia (1983) at landfall. *Monthly Weather Review*, *115*(1), 75–99. https://doi.org/10.1175/1520-0493(1987)115⟨0075:CITLLK⟩2.0.CO;2

Powell, M., & Reinhold, T. A. (2007). Tropical cyclone destructive potential by integrated kinetic energy. *Bulletin of the American Meteorological Society*, *88*(4), 513–526. https://doi.org/10.1175/bams-88-4-513

Prat, O. P., & Nelson, B. R. (2013). Mapping the world's tropical cyclone rainfall contribution over land using the TRMM multi-satellite precipitation analysis. *Water Resources Research*, *49*(11), 7236–7254. https://doi.org/10.1002/wrcr.20527

Prather, M., Flato, G., Friedlingstein, P., Jones, C., Lamarque, J., Liao, H., & Rasch, P. (2013). Annex II: Climate system scenario tables. *Climate Change*, 1395–1445.

Price-Whelan, A. M., Price-Whelan, A. M., Sipőcz, B. M., Günther, H. M., Lim, P. L., Crawford, S. M., et al. (2018). The astropy project: Building an open-science project and status of the v2.0 core package. *The Astronomical Journal*, *156*(3), 123. https://doi.org/10.3847/1538-3881/aabc4f

Rasmussen, R., Liu, C., Ikeda, K., Gochis, D., Yates, D., Chen, F., et al. (2011). High-resolution coupled climate runoff simulations of seasonal snowfall over Colorado: A process study of current and warmer climate. *Journal of Climate*, *24*(12), 3015–3048. https://doi.org/10.1175/2010jcli3985.1

Reddy, J. P., Sriram, D., Gunthe, S. S., & Balaji, C. (2021). Impact of climate change on intense Bay of Bengal tropical cyclones of the post-monsoon season: A pseudo global warming approach. *Climate Dynamics*, *56*(9), 2855–2879. https://doi.org/10.1007/s00382-020-05618-3

Redmond, G., Hodges, K. I., McSweeney, C., Jones, R., & Hein, D. (2014). Projected changes in tropical cyclones over Vietnam and the South China Sea using a 25 km regional climate model perturbed physics ensemble. *Climate Dynamics*, *45*(7–8), 1983–2000. https://doi.org/10.1007/s00382-014-2450-8

Rego, J. L., & Li, C. (2009). On the importance of the forward speed of hurricanes in storm surge forecasting: A numerical study. *Geophysical Research Letters*, *36*(7), 96. https://doi.org/10.1029/2008GL036953

Ritchie, E. A., Wood, K. M., Gutzler, D. S., & White, S. R. (2011). The influence of eastern Pacific tropical cyclone remnants on the southwestern United States. *Monthly Weather Review*, *139*(1), 192–210. https://doi.org/10.1175/2010mwr3389.1

Rodgers, E. B., Adler, R. F., & Pierce, H. F. (2001). Contributions of tropical cyclones to the North Atlantic climatological rainfall as observed from satellites. *Journal of Applied Meteorology and Climatology*, *40*(11), 1785–1800. https://doi.org/10.1175/1520-0450(2001)040<1785:cotctt>2.0.co;2

Schär, C., Frei, C., Lüthi, D., & Davies, H. C. (1996). Surrogate climate-change scenarios for regional climate models. *Geophysical Research Letters*, *23*(6), 669–672. https://doi.org/10.1029/96GL00265

Seneviratne, S. I., Zhang, X., Adnan, M., Badi, W., Dereczynski, C., Di Luca, A., et al. (2021). Weather and climate extreme events in a changing climate. In *Climate change 2021: The physical science basis. Contribution of working group I to the sixth assessment report of the intergovernmental panel on climate change (technical report).*

Shapiro, L. J. (1983). The asymmetric boundary layer flow under a translating hurricane. *Journal of the Atmospheric Sciences*, *40*(8), 1984–1998. https://doi.org/10.1175/1520-0469(1983)040⟨1984:Tablfu⟩2.0.Co;2

Skamarock, W. C., Klemp, J. B., Dudhia, J., Gill, D. O., Liu, Z., Berner, J., et al. (2019). A description of the advanced research WRF model version 4 (Vol. *NCAR/TN-556+STR*). https://doi.org/10.5065/1dfh-6p97

Sobel, A. H., Wing, A. A., Camargo, S. J., Patricola, C. M., Vecchi, G. A., Lee, C.-Y., & Tippett, M. K. (2021). Tropical cyclone frequency. *Earth's Future*, *9*(12), e2021EF002275. https://doi.org/10.1029/2021EF002275

Storch, H. V., Langenberg, H., & Feser, F. (2000). A spectral nudging technique for dynamical downscaling purposes. *Monthly Weather Review*, *128*(10), 3664–3673. https://doi.org/10.1175/1520-0493(2000)128⟨3664:asntfd⟩2.0.co;2

Sun, Y., Zhong, Z., Li, T., Yi, L., Hu, Y., Wan, H., et al. (2017). Impact of ocean warming on tropical cyclone size and its destructiveness. *Scientific Reports*, *7*(1), 8154. https://doi.org/10.1038/s41598-017-08533-6

Takahashi, H. G., & Yasunari, T. (2008). Decreasing trend in rainfall over indochina during the late summer monsoon: Impact of tropical cyclones. *Journal of the Meteorological Society of Japan Series II*, *86*(3), 429–438. https://doi.org/10.2151/jmsj.86.429

Touma, D., Stevenson, S., Camargo, S. J., Horton, D. E., & Diffenbaugh, N. S. (2019). Variations in the intensity and spatial extent of tropical cyclone precipitation. *Geophysical Research Letters*, *46*(23), 13992–14002. https://doi.org/10.1029/2019GL083452

Tran, T. L., Ritchie, E. A., & Perkins-Kirkpatrick, S. E. (2022). A 50-year tropical cyclone exposure climatology in Southeast Asia. *Journal of Geophysical Research: Atmospheres*, *127*(4), e2021JD036301. https://doi.org/10.1029/2021JD036301

Trenberth, K. E., Cheng, L., Jacobs, P., Zhang, Y., & Fasullo, J. (2018). Hurricane Harvey links to ocean heat content and climate change adaptation. *Earth's Future*, *6*(5), 730–744. https://doi.org/10.1029/2018EF000825

Tsou, C. H., Huang, P. Y., Tu, C. Y., Chen, C. T., Tzeng, T. P., & Cheng, C. T. (2016). Present simulation and future typhoon activity projection over western north Pacific and Taiwan/east coast of China in 20-km HiRam climate model. *Terrestrial, Atmospheric and Oceanic Sciences*, *27*(5), 687–703. https://doi.org/10.3319/TAO.2016.06.13.04

Tsuboki, K., Yoshioka, M. K., Shinoda, T., Kato, M., Kanada, S., & Kitoh, A. (2015). Future increase of supertyphoon intensity associated with climate change. *Geophysical Research Letters*, *42*(2), 646–652. https://doi.org/10.1002/2014GL061793

Tu, S., Xu, J., Chan, J. C. L., Huang, K., Xu, F., & Chiu, L. S. (2021). Recent global decrease in the inner-core rain rate of tropical cyclones. *Nature Communications*, *12*(1), 1948. https://doi.org/10.1038/s41467-021-22304-y

United Nations (2021). Resilience in a riskier world: Managing systemic risks from biological and other natural hazards (technical report). Retrieved from https://www.unescap.org/kp/2021/asia-pacific-disaster-report-2021

Villarini, G., Lavers, D. A., Scoccimarro, E., Zhao, M., Wehner, M. F., Vecchi, G. A., et al. (2014). Sensitivity of tropical cyclone rainfall to idealized global-scale forcings. *Journal of Climate*, *27*(12), 4622–4641. https://doi.org/10.1175/jcli-d-13-00780.1

Waple, A., Lawrimore, J., Lyon, B., Halpert, M., Gleason, K., Menne, M., et al. (2002). Climate assessment for 2001. AGU spring meeting abstracts-1, 01. https://doi.org/10.1175/1520-0477(2002)083⟨0938:CAF⟩2.3.CO;2

Wilcoxon, F. (1992). Individual comparisons by ranking methods. In *Breakthroughs in statistics* (pp. 196–202). Springer.

Wood, K. M., & Ritchie, E. A. (2013). An updated climatology of tropical cyclone impacts on the southwestern United States. *Monthly Weather Review*, *141*(12), 4322–4336. https://doi.org/10.1175/mwr-d-13-00078.1

Wu, L., Chou, C., Chen, C. T., Huang, R., Knutson, T. R., Sirutis, J. J., et al. (2014). Simulations of the present and late-twenty-first-century western north Pacific tropical cyclone activity using a regional model. *Journal of Climate*, *27*(9), 3405–3424. https://doi.org/10.1175/JCLI-D-12-00830.1

Yamada, Y., Satoh, M., Sugi, M., Kodama, C., Noda, A. T., Nakano, M., & Nasuno, T. (2017). Response of tropical cyclone activity and structure to global warming in a high-resolution global nonhydrostatic model. *Journal of Climate*, *30*(23), 9703–9724. https://doi.org/10.1175/jcli-d-17-0068.1